EUROPEAN ORGANIZATION FOR NUCLEAR RESEARCH

Measurement of inclusive b-jet production in pp and p–Pb collisions at $\sqrt{s_{\mathrm{NN}}} = 5.02$ TeV

ALICE Collaboration[*]

Abstract

A measurement of the inclusive b-jet production cross section is presented in pp and p–Pb collisions at $\sqrt{s_{\mathrm{NN}}} = 5.02$ TeV using data collected with the ALICE detector at the LHC. The jets were reconstructed in the central rapidity region $|\eta| < 0.5$ from charged particles using the anti-k_{T} algorithm with resolution parameter $R = 0.4$. Identification of b jets exploits the long lifetime of b hadrons based on the properties of secondary vertices and impact parameter distributions. The production yields of tagged jets were corrected for tagging efficiency, purity, detector effects, and contribution from the underlying event background. The p_{T}-differential inclusive production cross section of b jets, as well as the corresponding inclusive b-jet fraction, are reported for p–Pb and pp collisions in the jet transverse momentum range $10 \leq p_{\mathrm{T,ch\,jet}} \leq 100$ GeV/c together with the nuclear modification factor, $R_{\mathrm{pPb}}^{\mathrm{b\text{-}jet}}$. The nuclear modification factor is found to be consistent with unity, indicating that the production of b jets in p–Pb at $\sqrt{s_{\mathrm{NN}}} = 5.02$ TeV is not affected by cold nuclear matter effects within the current precision. The measurements are well reproduced by POWHEG NLO pQCD calculations with PYTHIA fragmentation.

---

[*]See Appendix A for the list of collaboration members

1   Introduction

At extremely high energy densities and temperatures, which occur in ultra-relativistic heavy-ion collisions, nuclear matter transforms into its hot and dense deconfined phase, the Quark-Gluon Plasma (QGP) [1–3]. In the domain of vanishing baryon number, the QGP was found to be a strongly coupled state of matter, exhibiting significant collectivity [4–7]. Properties of this medium can be probed with jets, collimated showers of particles produced by fragmentation and hadronization of hard scattered partons [8, 9]. Interaction of the initial partonic shower with the medium proceeds via collisional and radiative processes which cause energy dissipation and its redistribution inside the partonic shower. This results in the suppression of high transverse momentum (p_T) hadrons and jets [10–14] in nucleus-nucleus collisions relative to proton-proton (pp) collisions, the so-called jet quenching, as well as in the modification of the jet substructure [15–18]. The suppression can be quantified by means of the nuclear modification factor, obtained as a ratio of the particle or jet yield measured in nucleus-nucleus collisions and the expected yield that would be obtained from a superposition of independent pp collisions.

Small collision systems such as pp or p–A are studied, besides for providing the natural reference for the more complex nucleus-nucleus collisions, also to look for an onset of QGP-like effects. These systems indeed represent an important test bench for theoretical models which describe a heavy-ion collision process as they bring information about the system-size evolution of the QGP signatures, as well as cold nuclear matter (CNM) effects, such as the modification of the parton distribution functions in nuclei (nPDF) by (anti-)shadowing or by gluon saturation, k_T-broadening by multiple soft scatterings, and energy loss in the cold nuclear matter [19–22]. Understanding CNM effects is essential for the accurate quantification of the effects of a hot and dense medium in heavy-ion measurements. Experimental studies of small collision systems at the LHC and RHIC revealed significant azimuthal correlations between particles with a large pseudorapidity separation in high-multiplicity pp and p–Pb, as well as in p–Au and d–Au collisions [23–25]. This behavior resembles the collectivity seen in larger collision systems. Yet, it is still an open question whether this phenomenon stems from complex quantum chromodynamics (QCD) effects such as interactions of color strings or QCD interference, or from the presence of a QGP droplet [26–29], as the measured nuclear modification factor of high-p_T hadrons and jets in minimum bias p–Pb events does not exhibit any evidence of jet quenching within the precision of the current measurements [30–33].

Jet quenching and CNM effects can be studied with heavy-flavor b and c quarks which are abundantly produced at the LHC energies. Heavy-flavor quarks provide a unique opportunity to study several aspects of QCD ranging from their production in hard partonic scattering processes, described with perturbative QCD, to the mass dependent energy loss [34–37] and collective motion [38, 39] inside the strongly-interacting medium created in collision systems of various sizes, coalescence of heavy and light quarks, as well as the mass-dependence of jet fragmentation [40–42]. Due to these effects, the sensitivity of heavy-flavor probes to the presence of hot or cold nuclear matter can be expected to differ from that of light-flavor probes. While a flavor-mass hierarchy of jet quenching was observed in Pb–Pb collisions [43–45], recent measurements of charm jets, D mesons, and heavy-flavor decay electrons in p–Pb do not show any evidence of nuclear modification [33, 46, 47].

The vast majority of heavy-flavor quarks is produced in initial hard processes. Due to their small annihilation cross sections and long decay times, their number is approximately conserved in the later stages of the reaction. Hadronization of heavy-flavor quarks then produces open heavy-flavor hadrons, which can be reconstructed directly through their weak hadronic decays or indirectly via their leptonic decay channels. The reconstruction of jets containing heavy-flavor hadrons, however, provides a more direct access to the primary heavy-flavor parton kinematics. By measuring heavy-flavor jets, production and fragmentation effects can be studied separately. Charm-tagged jets have been measured by ALICE in pp collisions at $\sqrt{s} = 7\,\text{TeV}$ [48]. Previous measurements of b jets in pp and p–Pb collisions were performed by the CMS experiment [49] at the LHC. CMS reported the nuclear modification factor for b

68 jets with transverse momentum larger than 50 GeV/c and the results do not exhibit any suppression. The
69 ALICE detector has excellent tracking capabilities for low-p_T charged particles, which makes it possible
70 to measure b jets at relatively low transverse momenta. This provides a unique opportunity at the LHC
71 to study nuclear modification of b jets down to the region where the jet energy scale is of similar mag-
72 nitude compared to the b quark mass, which increases sensitivity to the mass dependent effects. In this
73 paper, we present the first measurement of inclusive charged-particle b-jet p_T-differential cross section
74 and the b-jet fraction down to jet-transverse momentum $p_{T,\text{ch jet}} = 10$ GeV/c in p–Pb and pp collisions at
75 $\sqrt{s_{NN}} = 5.02$ TeV. The measured p_T distributions were used to obtain the nuclear modification factor
76 of b jets, $R_{\text{pPb}}^{\text{b-jet}}$, in the transverse momentum range $10 \leq p_{T,\text{ch jet}} \leq 100$ GeV/c.

77 The paper is organized as follows: the next section introduces the experimental setup and data sets
78 used for these measurements. Jet reconstruction and the b-jet tagging procedures are described in Sec. 3.
79 Section 4 deals with correction steps that were applied in the analysis. These include corrections for b-jet
80 tagging efficiency, b-jet tagging purity, and unfolding of the jet momentum smearing due to underlying
81 event fluctuations and instrumental effects. Systematic uncertainties are discussed in Sec. 5. Section 6 is
82 devoted to the discussion of the final results. The paper is summarized in Sec. 7.

2 Experimental setup and datasets

84 The ALICE detector [50, 51] consists of a central barrel, a forward muon arm, and a few other for-
85 ward detectors that are used for triggering and event characterization. The central barrel hosts detection
86 systems that provide tracking and particle identification. The most important ones for this analysis are
87 the Inner Tracking System (ITS) and the Time Projection Chamber (TPC). The ITS is a 6-layer silicon
88 tracker, which allows for precise reconstruction of primary interaction and secondary decay vertices. All
89 subdetectors of the central barrel are placed in a solenoidal magnetic field of 0.5 T.

90 The main triggering device is the V0 detector [52]. The V0 consists of two scintillator arrays V0A and
91 V0C covering full azimuth and forward and backward pseudorapidity ranges $2.8 < \eta < 5.1$ and $-3.7 <$
92 $\eta < -1.7$, respectively. The minimum bias trigger (MB) is defined by a coincidence of V0A and V0C
93 signals. The cross section of interactions resulting in a MB trigger was determined by a van der Meer
94 scan and it is $\sigma_{V0} = 2.09 \pm 0.07$ b for p–Pb collisions at $\sqrt{s_{NN}} = 5.02$ TeV [53] and $\sigma_{V0} = 51.2 \pm 1.2$ mb
95 for pp collisions at $\sqrt{s} = 5.02$ TeV [54].

96 The present analysis is based on the p–Pb and pp collisions at $\sqrt{s_{NN}} = 5.02$ TeV taken by ALICE in
97 2016 and 2017, respectively. For p–Pb collisions, the beam energies of colliding protons and Pb nuclei
98 were asymmetric: the protons had 4 TeV, while Pb nuclei had an energy of 1.59 TeV per nucleon. This
99 resulted in the laboratory frame in a rapidity (y) shift of the nucleon-nucleon center-of-mass system by
100 $\Delta y = 0.465$ in the direction of the proton beam.

101 The events were selected using the MB trigger. The p–Pb data set corresponds to an integrated luminosity
102 of 291 μb^{-1} (609×10^6 MB events) and the pp data set to 18 nb^{-1} (924×10^6 MB events). Only events
103 with position of the reconstructed primary vertex along the beam axis within $|z_{\text{vtx}}| < 10$ cm were retained
104 to assure a uniform detector coverage at midrapidity. The background from beam-gas interactions and
105 pileup events was rejected by using a correlation between the V0 detector and ITS signals. Residual
106 pileup events with identified primary interaction vertices separated by more than 0.8 cm were further
107 rejected.

3 Jet reconstruction and b-jet identification

109 The analysis uses high-quality tracks [48] reconstructed in the pseudorapidity range $|\eta_{\text{track}}| < 0.9$ that
110 have at least one hit in either of the two innermost layers of the ITS, the so called Silicon Pixel Detec-
111 tor (SPD). In the regions where the SPD was inefficient, high-quality tracks were supplemented with

complementary tracks that do not have a hit in the SPD to achieve azimuthal uniformity in the tracking acceptance. Momentum resolution of complementary tracks is improved by constraining the origin of the track to the primary vertex point. Complementary tracks constitute about 3.5% of all primary tracks. Tracking efficiency for primary tracks with $p_T > 1$ GeV/c varies with p_T between 70 and 85%. Primary-track momentum resolution is about 0.7% at $p_T = 1$ GeV/c, 1.6% at $p_T = 10$ GeV/c, and 4% at $p_T = 50$ GeV/c. The spatial resolution of the track impact parameter with respect to the primary vertex is better than 75 μm for charged-particle tracks with transverse momentum $p_T > 1$ GeV/c [48]. More information about the track selection can be found in Ref. [48].

Jets were reconstructed using the infrared and collinear safe anti-k_T algorithm [55] from the FastJet package [56]. The resolution parameter was set to $R = 0.4$, which ensures that most of the momentum of the initial parton (approximately 70% to 90% in the range of the current measurement) falls within the jet cone [57]. The jets were constructed from charged particles having $p_{T,track} > 0.15$ GeV/c and pseudorapidity $|\eta_{track}| < 0.9$. Their four-momenta were combined using the p_T recombination scheme, which considers all particles to be massless [56]. The pseudorapidity coverage of the reconstructed jets was constrained to $|\eta_{jet}| < 0.9 - R = 0.5$ to select only jets that are fully contained within the TPC acceptance.

The reconstructed transverse momentum for jets $p_{T,chjet}^{reco}$ is obtained using the measured transverse momentum of jets from charged particles $p_{T,chjet}^{raw}$ corrected for the mean contribution of the underlying event using the formula [58]

$$p_{T,chjet}^{reco} = p_{T,chjet}^{raw} - \rho \cdot A_{jet}.$$ (1)

Here A_{jet} denotes the area of the jet and ρ is the mean underlying event p_T density. The mean underlying event p_T density was calculated on event-by-event basis using the estimator introduced by CMS [59]. The CMS estimator is convenient for sparse systems like pp or p–Pb and defines the ρ as

$$\rho = \text{Median}_{k_T \text{ jets}} \left\{ \frac{p_{T,chjet,i}^{raw}}{A_{jet,i}} \right\} \cdot C, \quad \text{where} \quad C = \frac{\text{Covered Area}}{\text{Total Area}}.$$ (2)

Here the index i runs over a set of k_T jets [60] with $R = 0.4$ and $p_{T,chjet}^{raw} > 0.15$ GeV/c. The charged-track occupancy factor C accounts for the fraction of acceptance which is covered by charged-particle jets.

Identification of b-jets is based on kinematic variables related to the relatively long lifetime of b hadrons and large impact parameter of beauty-hadron-decay daughters. Several discriminator variables were defined and applied in two distinct b-jet tagging methods that are presented in this paper, the impact parameter (IP) method (based on the distance of closest approach DCA of tracks to the primary vertex), and the displaced secondary vertex (SV) method (based on the topology of the reconstructed secondary vertices). Both methods are discussed in detail below. For more information on b-jet tagging algorithms, the reader may refer to Refs. [61–63].

3.1   b-jet tagging based on impact parameter

The impact parameter can be measured either in three dimensions or in the projection on the plane perpendicular to the beam axis. This analysis used the latter definition (denoted d_{xy}) due to poor DCA resolution along the beam axis.

The sign of the impact parameter is determined as the sign of the scalar product of the jet axis and the impact parameter vector pointing from the primary vertex to the point of closest approach. Tracks originating from a secondary vertex tend to have positive impact parameter values because of the mother particle decay length. On the other hand, the tracks originating from the primary vertex can have both positive and negative impact parameter values due to finite resolution, which smears impact parameters of primary tracks symmetrically around the primary vertex. Discrimination among different jet flavors was based on impact parameter significance (Sd_{xy}), defined as the ratio of the impact parameter over

its estimated uncertainty (resolution). The impact parameter resolution largely depends on the η and the p_{T} of the tracks. Figure 1 (top left) shows the probability distribution of the impact parameter significance for tracks belonging to different jet flavors, as determined from PYTHIA 8 Monash 2013 tune [64] detector-level Monte Carlo (MC) simulations which calculate particle transport through the ALICE apparatus using GEANT 3 [65]. On average, tracks of b jets have larger Sd_{xy} values when compared to c jets and light-flavor jets. This means that the impact parameter has a strong discriminating power in distinguishing between the different jet flavors.
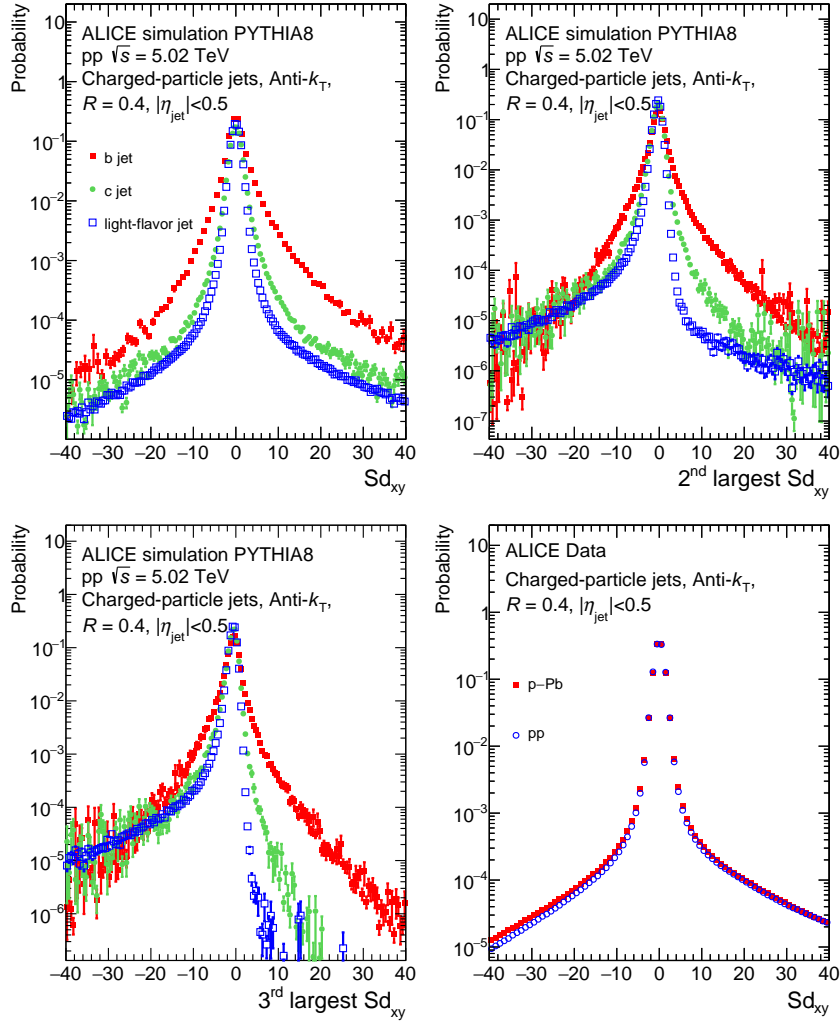

Figure 1: *Top left:* The normalized distribution of the impact parameter significance for all tracks inside light-flavor, charm, and beauty jets as determined from PYTHIA 8 (Monash 2013 tune [64]) detector-level simulations. *Top right:* The distribution for the second largest impact parameter significance in the jet. *Bottom left:* The distribution of the third largest Sd_{xy} in the jet. *Bottom right:* The distribution of the impact parameter significance Sd_{xy} for data in pp and p–Pb collisions.

In the analysis, the track counting algorithm [61] arranges the Sd_{xy} values of tracks in a jet in descending order. A jet was tagged as a b jet if the second largest impact parameter significance (see Fig. 1 top right) value was greater than a certain threshold parameter $Sd_{xy}^{\min}$. The default threshold parameter that was chosen in this analysis is $Sd_{xy}^{\min} = 2.5$ which gives an average tagging efficiency of 55% with average purity of 42% for b-jets with $20 < p_{\mathrm{T,ch\,jet}}^{\mathrm{reco}} < 40\,\mathrm{GeV}/c$. This choice provided an optimum between good efficiency and good background rejection. Discriminations based on the tracks with the first largest as well as the third largest impact parameter significance (see Fig. 1 bottom left) value were used for

6

168 consistency checks.

169 The efficiency of the b-jet tagging and the purity of the selected b-jet sample presented in Sec. 4.1 were
170 determined using the jet probability algorithm [61, 63, 66]. This algorithm evaluates a combined impact
171 parameter significance of tracks inside the jet and estimates a likelihood that all tracks associated with
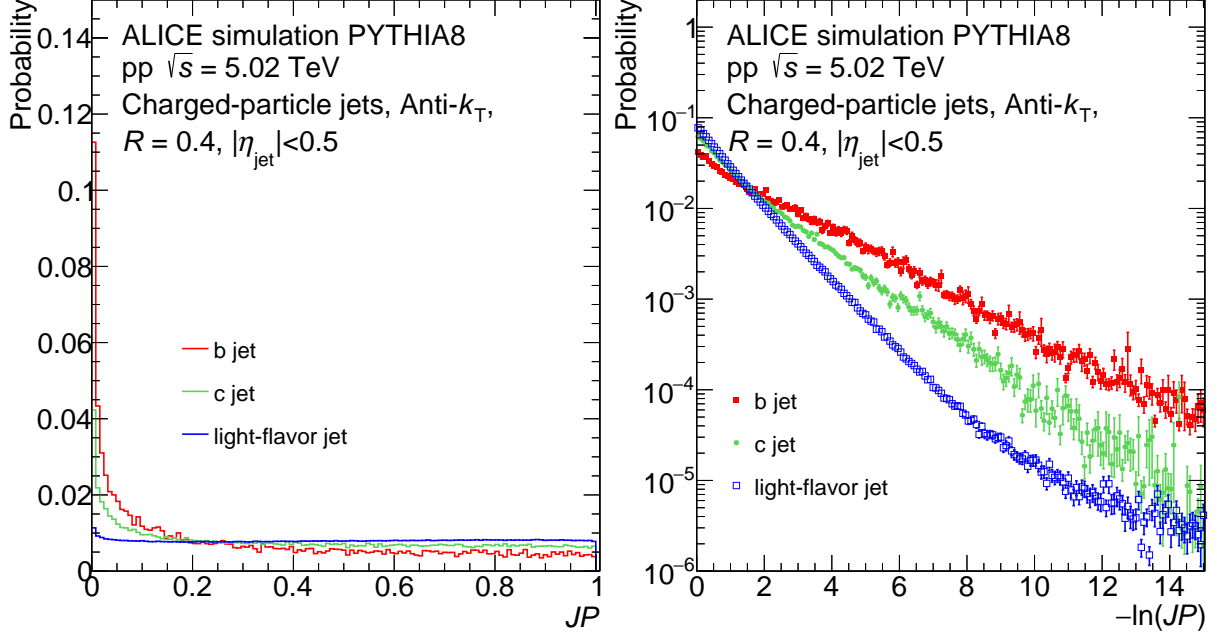172 the jet originated from the primary vertex.

Figure 2: left: Jet probability distribution for light-flavor, charm, and beauty jets in pp collisions at $\sqrt{s} = 5.02$ TeV. Right: The logarithmic jet probability $-\ln(JP)$ for different jet flavors.

173 The algorithm defines a resolution function R_{IP} by fitting the negative side of the signed Sd_{xy} distribution
174 (bottom right panel of Fig. 1). The fit is carried out on the negative part of the distribution, because in this
175 range it is predominantly populated by primary tracks originating from the primary vertex. The resolution
176 function was separately obtained for seven different track categories, which classify all reconstructed
177 tracks according to possible geometric and tracking effects. Tracks were assigned to these categories
178 according to their number of hits in the ITS, χ^2/NDF of the track fits, and track p_{T}.

179 The resolution functions corresponding to the different track categories were used to calculate the so
180 called track probability, P_{tr}, which corresponds to the probability that a high-quality jet constituent track
181 with an impact parameter significance Sd_{xy} is coming from the primary vertex:

$$P_{\mathrm{tr}}(Sd_{xy}) = \frac{\int_{-\infty}^{-|Sd_{xy}|} R_{\mathrm{IP}}(S)\mathrm{d}S}{\int_{-\infty}^{0} R_{\mathrm{IP}}(S)\mathrm{d}S} \, , \tag{3}$$

182 where the integration is done over the negative side of the impact parameter significance distribution. A
183 large impact parameter value results in a small P_{tr} that a track is coming from the primary vertex.

184 The jet probability (JP) is then calculated by combining the P_{tr} values of tracks inside the given jet
185 according to the equation [61, 63, 66]:

$$JP = \prod \times \sum_{k=0}^{N_{\mathrm{track}}-1} \frac{(-\log\prod)^k}{k!} \, , \text{where} \quad \prod = \prod_{i=1}^{N_{\mathrm{track}}} P_{\mathrm{tr},i} \, . \tag{4}$$

186 Only tracks with positive Sd_{xy} are selected to calculate the jet probability. Figure 2 left shows the JP
187 probability distribution for the different jet flavors. The fist bin of the JP distribution is dominated by

jets in which tracks do not origin from the primary vertex. Such jets are mostly b and c jets. Indeed, one can see that the *JP* distribution for b jets peaks at *JP* = 0 and turns out to be almost flat for *JP* > 0.2. A similar but smaller peak is visible also in the c-jet *JP* distribution. In contrast, the *JP* distribution of light-flavor jets is almost flat in the whole range.

As can be seen in Fig. 2 left, the *JP* discriminates the different jet flavors only in a very narrow interval ($0 < JP < 0.2$). This distribution is therefore not convenient for template fitting. For this reason, the $-\ln(JP)$ quantity was used as a discriminator in our analysis to determine the b-jet tagging efficiency with a data-driven method. As shown in Fig. 2, the $-\ln(JP)$ drops much faster for light-flavor jets and c jets when compared to b jets, allowing for an effective statistical discrimination of b jets.

3.2   b-jet tagging based on secondary vertex reconstruction

The secondary vertices (SV) of beauty hadron decays are in most cases well displaced from the primary vertex of the collision, owing to the relatively long lifetime of beauty hadrons ($c\tau \approx 500\,\mu$m). The decay of beauty hadrons then mostly gives birth to non-prompt charm particles which typically have a similarly long lifetime ($c\tau \approx 100$ to $300\,\mu$m). The SV algorithm reconstructs the secondary vertices inside the jets from triplets of jet-constituent tracks. Out of all of the reconstructed secondary vertices, this algorithm selects the most displaced vertex for the b-jet tagging. The vertex reconstruction quality is described by the dispersion of the reconstructed secondary vertex, $\sigma_{\mathrm{SV}} = \sqrt{d_1^2 + d_2^2 + d_3^2}$, where $d_{1,2,3}$ are the distances of closest approach of the three tracks to the secondary vertex.

This algorithm uses the decay length L_{xy} as a discriminator. The decay length is the distance between the primary vertex and the secondary vertex measured in the plane transverse to the beam axis. The significance is then defined by dividing L_{xy} by its uncertainty, $SL_{xy} = L_{xy}/\sigma_{L_{xy}}$. The b-tagging is then done by applying a cut on both the SV dispersion σ_{SV} and the decay length significance SL_{xy}.

The default operating point of the tagging cuts in the analysis is $SL_{xy} > 7$ and $\sigma_{\mathrm{SV}} < 0.03$ cm. These selection values were determined by optimizing for high b-tagging efficiency and low c-quark and light-flavor mistagging rates based on simulations. Figure 3 shows examples of the SL_{xy} and σ_{SV} distributions for jets having different flavor as obtained from PYTHIA 8 simulations using the Monash tune [64] followed by an ALICE detector level MC simulation and reconstruction. Figure 4 shows examples of the SL_{xy} and σ_{SV} probability distributions from pp and p–Pb collision data.
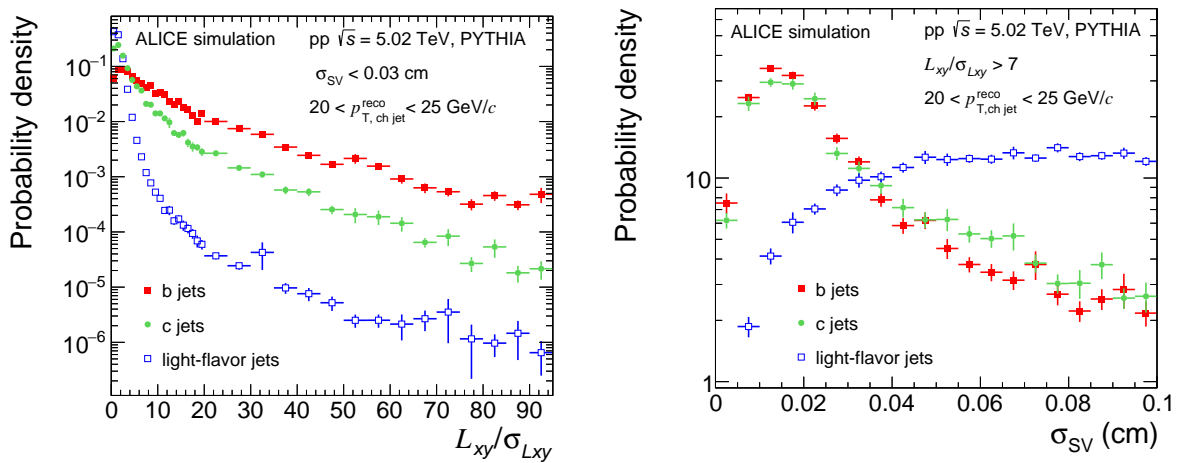

Figure 3: Distributions of the tagging discriminators used in the SV method, SL_{xy} (left) and σ_{SV} (right), for b jets, c jets, and light-flavor jets as obtained from a MC simulation of the ALICE apparatus, using PYTHIA as event generator.
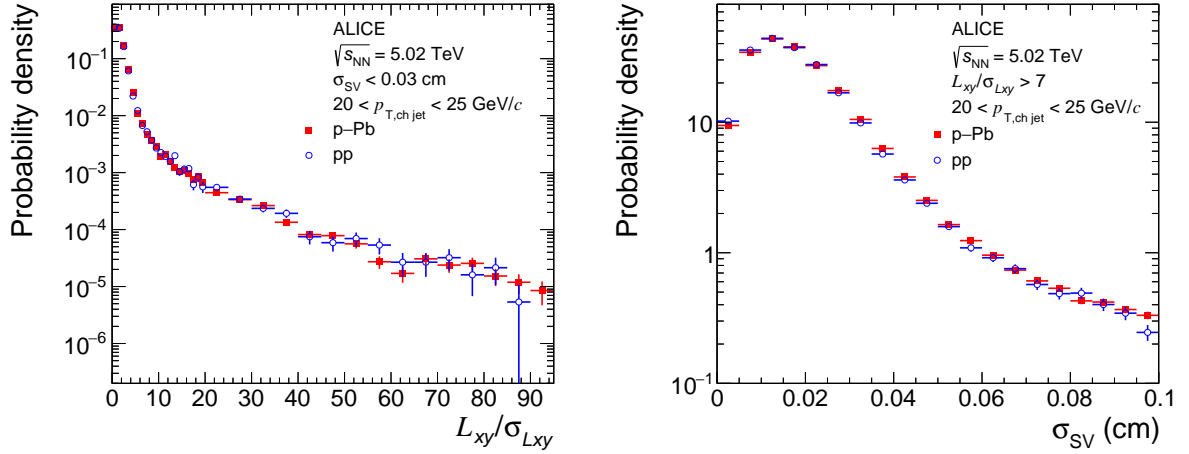
Figure 4: Distributions of the tagging discriminators used in the SV method, SL_{xy} (left) and σ_{SV} (right).

4   Corrections of the b-tagged jet spectrum

The raw p_T spectrum of b-jet candidates ($\mathrm{d}N^{\text{tagged}}/\mathrm{d}p_{\text{T,ch jet}}^{\text{reco}}$) that was obtained after applying the tagging algorithms, was corrected for the b-jet tagging efficiency, ε_b, and the purity of the selected b-jet sample, P_b,

$$\frac{\mathrm{d}N_{\text{det. level}}^{\text{b jet}}(p_T)}{\mathrm{d}p_{\text{T,ch jet}}^{\text{reco}}} = \frac{\mathrm{d}N^{\text{tagged}}}{\mathrm{d}p_{\text{T,ch jet}}^{\text{reco}}} \cdot \frac{P_b}{\varepsilon_b}. \tag{5}$$

The resulting spectrum is then corrected for momentum smearing due to detector effects and background fluctuations by means of unfolding. All corrections are discussed below in detail.

4.1   Tagging efficiency

The b-jet tagging algorithms discussed in Section 3 do not identify all produced b jets. The probability that a given tagging algorithm correctly identifies a jet originating from a b quark as a b jet is called the tagging efficiency. Similarly, one can also define the mistagging efficiency as a probability that a jet originating from a charm quark or a light-flavor parton will be falsely tagged as a b jet. The tagging and mistagging efficiencies of a given algorithm are defined as,

$$\varepsilon_i(p_T) = \frac{N_i^{\text{tagged}}(p_{\text{T,ch jet}}^{\text{reco}})}{N_i^{\text{total}}(p_{\text{T,ch jet}}^{\text{reco}})} , \tag{6}$$

where i is the jet flavor (b, c or light-flavor), N_i^{tagged} is the number of tagged i-jets, and N_i^{total} is the total number of i-jets.

4.1.1   Tagging efficiency of the IP algorithm

The tagging efficiency of the IP algorithm was estimated based on the semi-data-driven method outlined in Refs. [61, 67]. In this method, the $-\ln(JP)$ distributions are fitted with a set of detector-level MC templates, which describe the shape of the jet probability distributions corresponding to b jets, c jets, and light-flavor jets. The templates for p–Pb were obtained from a MC simulation based on the EPOS event generator [68] with embedded PYTHIA 6 events, propagated through a model of the ALICE detector via GEANT 3 [65]. The simulated events were then reconstructed as events in data. The templates for pp collisions were obtained similarly, using the PYTHIA 8 MC event generator.

Two jet samples were created: a sample that contains the jets satisfying the tagging requirement, and another sample that contains the inclusive jets before applying the tagging algorithm. The associated $-\ln(JP)$ distributions from data were fit with the corresponding b, c, and light-flavor jet templates using a binned maximum likelihood fit. The fitting procedure was done separately for the "tagged" jet (with $Sd_{xy}^{\min} = 2.5$) and the inclusive "untagged" jet samples, see Fig. 5.
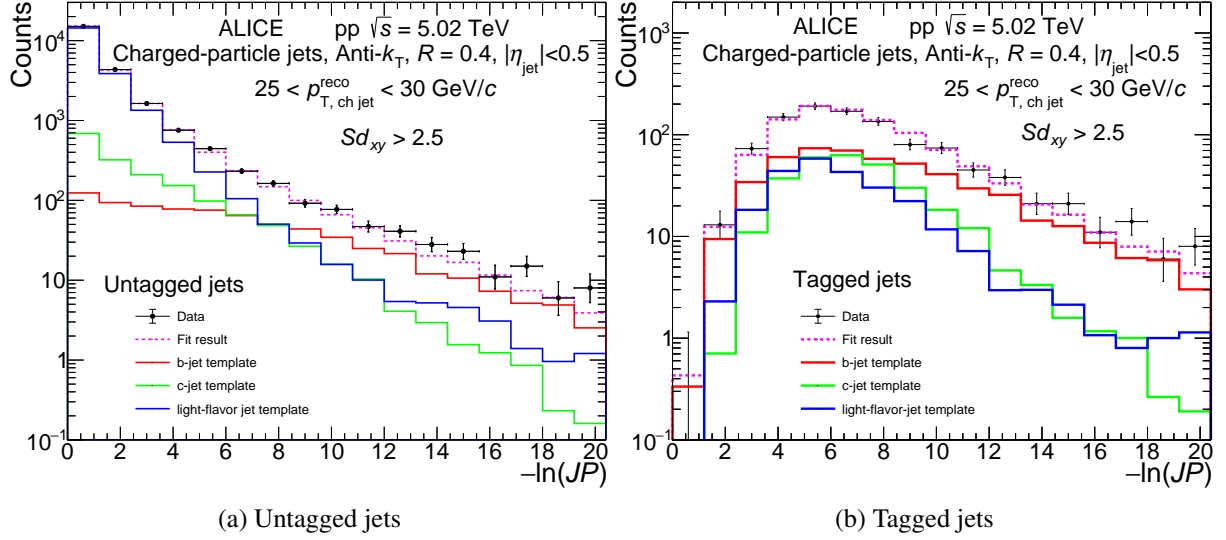

Figure 5: Fit of the measured $-\ln(JP)$ discriminator distribution with a linear combination of b, c, and light-flavor jet templates for the untagged sample (left) and for the tagged sample (right).

The b-jet tagging efficiency is then obtained as the ratio of the number of identified b jets to the number of b jets before identification:

$$\varepsilon_{\mathrm{b}} = \frac{C_{\mathrm{b}} \cdot f_{\mathrm{b}}^{\mathrm{tag}} \cdot N_{\mathrm{data}}^{\mathrm{tag}}}{f_{\mathrm{b}}^{\mathrm{untag}} \cdot N_{\mathrm{data}}^{\mathrm{untag}}} . \tag{7}$$

Here $f_{\mathrm{b}}^{\mathrm{untag}}$ and $f_{\mathrm{b}}^{\mathrm{tag}}$ denote the b-jet fractions before and after tagging, respectively, which are extracted from the fits; $N_{\mathrm{data}}^{\mathrm{untag}}$ and $N_{\mathrm{data}}^{\mathrm{tag}}$ give the numbers of jets before and after tagging, which were extracted from data; finally, C_{b} is the fraction of b-jets for which the jet probability can be defined, i.e. b jets having at least two constituent tracks with positive Sd_{xy}. This factor was estimated from MC. The C_{b} is about 80% at 10 GeV/c and increases until it reaches 98% at 40 GeV/c and stays like that for $p_T > 40$ GeV/c.

Figure 6 shows the b-jet tagging efficiency of the IP method in pp and p–Pb collisions. As an alternative for $-\ln(JP)$ in the template fitting, other discriminators were also used to check consistency and estimate the systematics. The alternative discriminators were the jet mass distribution [69] and the distribution of energy fraction f_E carried by the secondary vertex in the jet. Both of them provided results that are consistent with the standard analysis within one standard deviation. The systematic uncertainty on the tagging efficiency is estimated by fitting the f_E distribution instead of $-\ln(JP)$. Finally, it is worth noticing that the template fit procedure yields results with large systematical errors for $p_{\mathrm{T,chjet}} < 20$ GeV/c, so the interval between $10 < p_{\mathrm{T,chjet}} < 20$ GeV/c was omitted in the IP analysis.

4.1.2 Tagging efficiency of the SV algorithm

In case of the SV method, the tagging and mistagging efficiencies of beauty, charm, and light-flavor jets were estimated based on the same detector-level MC simulation data sets that were used by the IP method. While the IP algorithm used the MC simulation to get templates and assessed the reconstruction efficiency by a semi-data-driven method, in the SV algorithm the efficiency was obtained directly from the MC simulation via Eq. (6). In the particle-level simulations, a jet was counted as a b jet if there
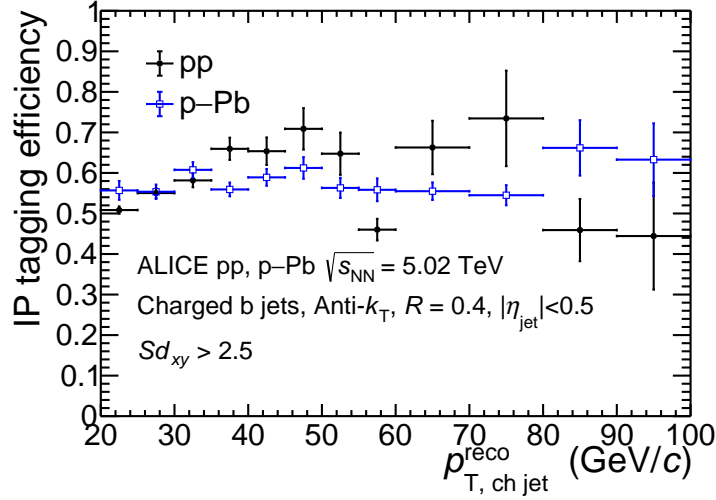
Figure 6: The b-jet tagging efficiency extracted from the data-driven method using the IP algorithm in pp and p–Pb collisions.

was a beauty hadron present with a three-momentum vector contained within the jet cone. Analogous definition was used also for c jets and the remaining jets were considered to be light-flavor jets. Figure 7 presents the efficiencies as a function of jet momentum in pp and p–Pb collisions. The figure shows that the tagging with the default tagging selection criteria yields similar performance in both systems, ensuring suppression of light-flavor jets by two orders of magnitude. Comparing the tagging efficiencies of the IP and SV methods, it can be seen that the efficiency of the IP method tagging is about a factor two higher.

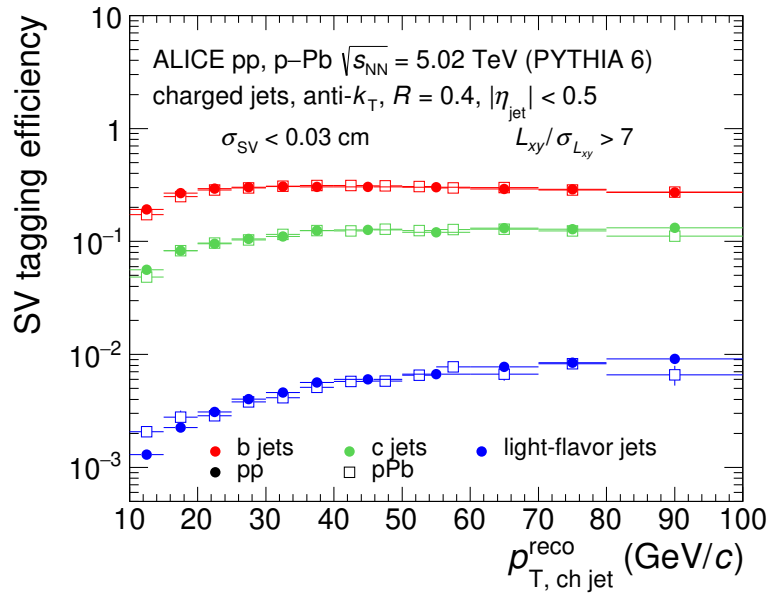

Figure 7: Tagging and mistagging efficiencies of beauty, charm, and light-flavor jets for the SV method in pp (solid markers) and p–Pb (open markers) collisions at $\sqrt{s_{NN}} = 5.02$ TeV, plotted as a function of jet transverse momentum.

11

4.2 Purity of the b-jet sample

The b-jet tagging algorithms introduced in Sec. 3 select not only b jets but also a certain fraction of charm and light-flavor jets, cf. Sec. 4.1. Given the higher production cross section of light-flavor and charmed jets, this leads to a significant sample contamination that needs to be corrected for. The purity of the tagged sample of b-jet candidates P_b is defined as the fraction of true b jets among the total number of tagged jets,

$$P_b(p_{\text{T,ch jet}}^{\text{reco}}) = \frac{N_{\text{b jet}}^{\text{tagged}}(p_{\text{T,ch jet}}^{\text{reco}})}{N^{\text{tagged}}(p_{\text{T,ch jet}}^{\text{reco}})} \ . \tag{8}$$

Here $N_{\text{b jet}}^{\text{tagged}}$ is the number of tagged true b jets and N^{tagged} is the number of all tagged jets. One of the biggest challenges in the b-jet analysis is to obtain a solid purity estimate.

4.2.1 b-jet purity from the IP tagging

In the IP method analysis, the b-jet purity is estimated using a data-driven method based on the jet probability discriminator. A linear combination of detector-level MC templates corresponding to pure beauty, charm, and light-flavor jets were fitted to the $-\ln(JP)$ distribution measured in data in a similar way as discussed in Sec 4.1. Figure 8 shows the resulting b-jet purity for the IP method with $Sd_{xy}^{\min} = 2.5$ in pp and p–Pb collisions. The template fitting procedure was repeated with other discriminators to assess the corresponding systematic uncertainty, as detailed in Sec 4.1.
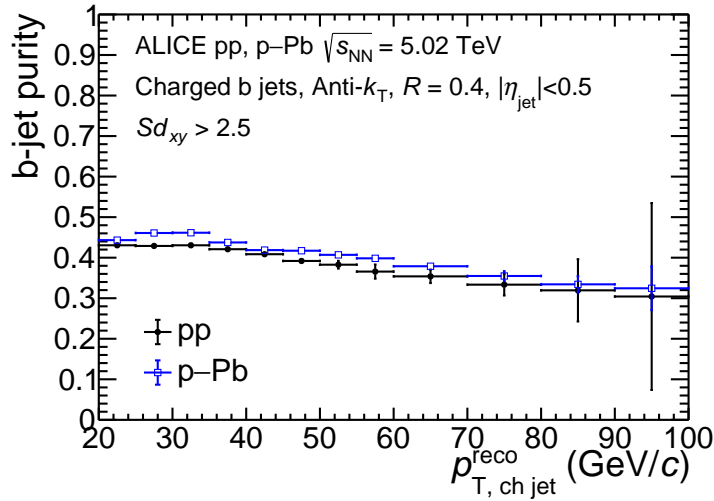

Figure 8: The b-jet purity as obtained from the IP method in pp and p–Pb collisions.

4.2.2 b-jet purity from the SV tagging

The purity of the b-jet candidate sample that was tagged with the SV method was estimated based on a hybrid method that utilizes both data-driven template fitting and simulations. In p–Pb data, the purities were primarily determined by fitting the invariant mass distribution of the most displaced secondary vertex with beauty, charm, and light-flavor templates. The invariant mass was calculated from the three prongs that were used to reconstruct the secondary vertex assuming that all tracks have the mass of a charged pion. These templates were obtained from the detector-level EPOS simulation with embedded PYTHIA 6 events. Analogous fits were done also for the pp data using detector-level PYTHIA templates. The fits were done in several p_T bins. Figure 9 shows a typical example of the template fit in pp and p–Pb collisions. The small statistical samples, however, prevented the use of the template fitting method for jets with momenta larger than 30–40 GeV/c. Therefore, the purity was also estimated based on POWHEG

HVQ simulations [70] with the CTEQ6M PDF set [71], and in the case of the p–Pb system, the EPS09 nPDF set in addition [72]. The simulated particle-level charm and beauty jet p_T spectra were subjected to instrumental (efficiency and detector effects) and background fluctuation effects to estimate the c- and b-jet contributions in the inclusive raw jet spectrum before tagging. The purity was then estimated in each $p_{T,chjet}^{reco}$ bin as follows,

$$P_b = \frac{\varepsilon_b N_b}{\varepsilon_b N_b + \varepsilon_c N_c + \varepsilon_{lf}(N_{incl} - N_b - N_c)}, \tag{9}$$

where ε_b, ε_c, and ε_{lf} are tagging and mistagging efficiencies for beauty, charm, and light-flavor jets, respectively; and N_b (N_c) is the estimated contribution of beauty (charm) jets in the raw inclusive un-tagged jets N_{incl}. This purity estimate nevertheless relies on model parameters that cannot be directly validated (quark masses as well as renormalization and factorization scales used in the computation of the beauty and the charm production cross-section). Hence a statistical analysis was carried out comparing the simulated purities with the purities obtained by the data-driven invariant mass template fit method simultaneously in a broad range of tagging cuts, to determine the simulation configurations that are consistent with the results of the data-driven method. Consistency was defined with a $\chi^2/\text{NDF} < 10$ goodness-of-description test taking into account the total number-of-degrees-of-freedom (NDF) in the simultaneous comparison. The configuration space covered variations of the QCD renormalization and factorization scales by factors 0.5–2 w.r.t. the default values, and variations of the quark masses in the range 4.5–5 GeV/c^2 for b and 1.3–1.7 GeV/c^2 for c quarks. The variation of the heavy quark masses only has a small effect on the observed b-jet sample purity (below 2% for the b quark and negligible for the c quark). Changing the factorization (renormalization) scales in the simulation of the b-quark spectrum with a factor of 2 affects the purity in the same (opposite) direction by 4 to 8%, while a factor of 2 change in the renormalization or factorization scales in the simulation of the c-quark spectrum may cause a 2 to 6% effect on the resulting purity in either direction.

The simulations with the accepted configurations were then used to determine the purities in the p–Pb as well as the pp data. Figure 10 shows a comparison of the b-jet sample purity obtained for the default tagging cuts with the template fit method and the POWHEG-simulation-based approach. All accepted configurations were used to assess the systematic uncertainty related to the purity of the tagged b-jet candidate sample.
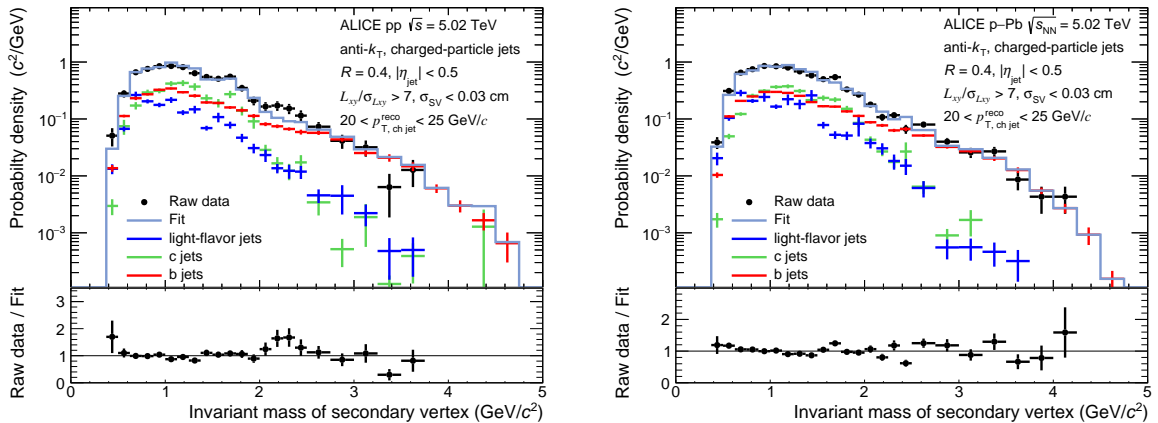
Figure 9: Invariant mass distribution of the combination of three prongs which form the most displaced secondary vertex in jets with $20 < p_{T,chjet}^{reco} < 30$ GeV/c tagged with the default selection $SL_{xy} > 7$ and $\sigma_{SV} < 0.03$ cm, for pp and p–Pb collisions. The data (black points) are fitted with detector-level MC templates corresponding to beauty, charm, and light-flavor jets to assess purity of the b-jet candidate sample. See the text for further information on the MC.

Figure 10: Purity of the b-jet candidates selected with the SV method when using the default tagging cuts. The purity was estimated with the data-driven template fit method (red points) and with the POWHEG-simulation based approach. The POWHEG scale variations accepted by the statistical analysis are colored green, the rejected ones are gray. Results for pp and p–Pb are shown in the left and right panel, respectively.

4.3 Detector effects and unfolding
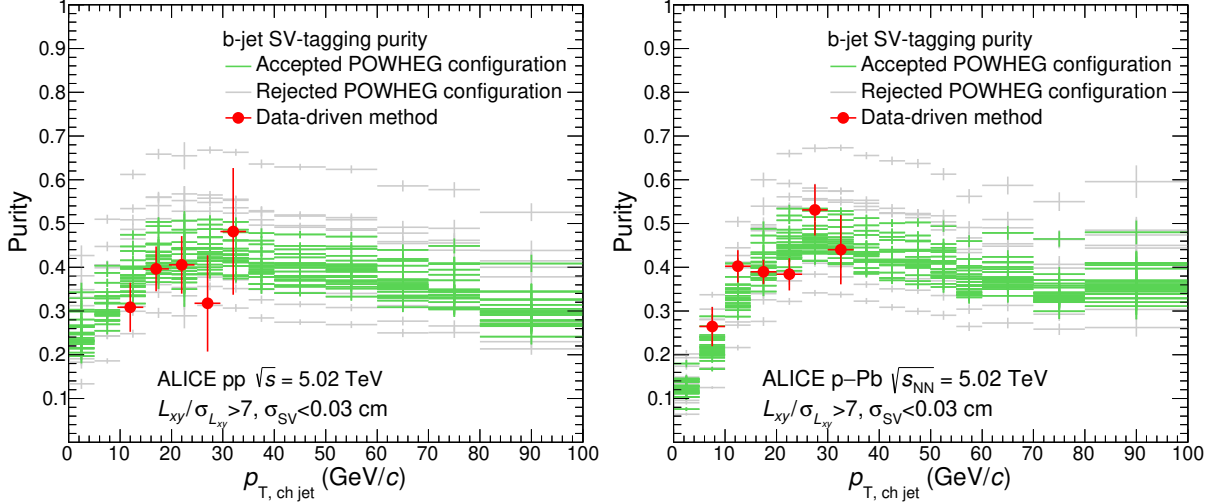
The measured jet spectra were affected by distortions stemming from two main sources: instrumental effects and local background fluctuations w.r.t. the mean underlying event density. These two effects smeared the true jet spectrum and can be corrected for via an unfolding procedure. The corrections were assumed to factorize and were handled with a product of two matrices that were determined separately [73]. The instrumental effects were accounted for by constructing a response matrix that is based on a b-jet sample generated with PYTHIA 8 [74], and subsequently processed with an ALICE GEANT 3-based particle transport model [65]. The detector-level jets were matched to the particle-level jets based on geometry, by minimizing their angular distance $\Delta R = \sqrt{\Delta\varphi^2 + \Delta\eta^2}$, where $\Delta\varphi$ and $\Delta\eta$ are azimuthal angle and pseudorapidity intervals between given particle-level and detector-level jets, respectively. One-to-one correspondence between particle-level and detector-level jets was required and ΔR was constrained to be less than 0.25 [75].

The matrix that describes momentum smearing due to background fluctuations was obtained with two methods based on track embedding and the random cone technique (RC) [76]. In the track embedding approach, a track was embedded perpendicular in azimuth to the axis of the tagged b-jet candidate. This region is expected to be dominated by the underlying event and the resulting momentum smearing is

$$\delta p_{\text{T}}^{\text{emb}} = p_{\text{T,chjet}}^{\text{raw,emb}} - \rho A_{\text{jet}} - p_{\text{T}}^{\text{emb}}, \tag{10}$$

where $p_{\text{T,chjet}}^{\text{raw,emb}}$ is the reconstructed momentum of the jet with the embedded track, A_{jet} is its area, ρ is the estimated underlying event p_{T} density, and $p_{\text{T}}^{\text{emb}}$ is the transverse momentum of the embedded track.

In the RC approach, momentum smearing was calculated using a cone with radius $R_{\text{cone}} = 0.4$ placed in a random position in the $\eta - \varphi$ plane in an event. This cone must not overlap with the leading and the sub-leading jets in the event and it has to be fully fitted inside the acceptance of the central barrel. The momentum smearing is calculated from tracks which are inside the cone as:

$$\delta p_{\text{T}}^{\text{RC}} = p_{\text{T}}^{\text{RC}} - \rho \pi R_{\text{cone}}^2, \tag{11}$$

where p_{T}^{RC} denotes the sum of track p_{T} inside the cone. Only events which contained a tagged b-jet candidate were selected for δp_{T} calculation.

348 The δp_{T} matrices obtained with the track embedding and RC techniques provided consistent unfolded
349 b-jet spectra and the remaining difference is accounted for as a systematic uncertainty. The IP analy-
350 sis considered the RC method in events with at least one tagged jet for the standard analysis and as a
351 systematic uncertainty the variation where the momentum smearing due to local underlying event fluc-
352 tuations was described with δp_{T} matrices obtained from inclusive events. In the SV analysis, the track
353 embedding technique was used in the standard analysis, and the RC method as a systematic variation.

354 The unfolding of the raw b-jet spectrum defined in Eq. (5) was by default carried out using the singular
355 value decomposition (SVD) method [77] implemented in the RooUnfold package [78]. The optimal reg-
356 ularization parameter value was found to be 4 for the SV analysis and 8 for the IP analysis. Stability of
357 the unfolded solutions was tested also with the Bayesian unfolding [79] and the χ^2 unfolding. These al-
358 gorithms provided consistent results with the SVD and the remaining differences were taken into account
359 in the systematic uncertainties.

4.4   b-jet cross section formula and nuclear modification factor

361 The p_{T}-differential b-jet production cross section was calculated as

$$\frac{\mathrm{d}^2\sigma^{\mathrm{b\,jet}}}{\mathrm{d}p_{\mathrm{T,ch\,jet}}\mathrm{d}\eta_{\mathrm{jet}}} = \frac{C_{\mathrm{vtx}}}{N_{\mathrm{evt}}} \cdot \sigma_{\mathrm{V0}} \cdot \frac{\mathrm{d}^2N^{\mathrm{b\,jet}}_{\mathrm{unfolded}}}{\mathrm{d}p_{\mathrm{T,ch\,jet}}\mathrm{d}\eta_{\mathrm{jet}}} \,, \tag{12}$$

362 where $\mathrm{d}^2N^{\mathrm{b\,jet}}_{\mathrm{unfolded}}/\mathrm{d}p_{\mathrm{T,ch\,jet}}\mathrm{d}\eta_{\mathrm{jet}}$ is the unfolded p_{T} differential yield of b jets, N_{evt} is the number of min-
363 imum bias events after event selection, and σ_{V0} is the total MB trigger cross section. The values of
364 N_{evt} and σ_{V0} for the pp and p–Pb data were quoted in Sec. 2. The vertex finding efficiency, C_{vtx}, was
365 measured to be 0.982 in p–Pb collisions and 0.948 in pp collisions. The C_{vtx} correction factor accounts
366 for those minimum bias events where the true primary vertex was within $|z_{\mathrm{vtx}}| < 10\,\mathrm{cm}$ but it was not
367 reconstructed. Such events do not contribute to N_{evt}, but they have to be considered for the absolute
368 normalization with respect to the measured MB cross section σ_{V0}.

369 Modification of the b-jet spectrum in p–Pb collisions due to nuclear matter effects was then quantified
370 with the nuclear modification factor, which compares the p_{T}-dependent production rates to expectation
371 from pp collisions

$$R^{\mathrm{b\text{-}jet}}_{\mathrm{pPb}} = \frac{1}{A} \frac{\mathrm{d}^2\sigma^{\mathrm{b\,jet}}_{\mathrm{pPb}}/\mathrm{d}p_{\mathrm{T,ch\,jet}}\mathrm{d}\eta_{\mathrm{jet}}}{\mathrm{d}^2\sigma^{\mathrm{b\,jet}}_{\mathrm{pp}}/\mathrm{d}p_{\mathrm{T,ch\,jet}}\mathrm{d}\eta_{\mathrm{jet}}} \,, \tag{13}$$

372 where A is the number of nucleons in the Pb nucleus, $\mathrm{d}^2\sigma^{\mathrm{b\,jet}}_{\mathrm{pPb}}/\mathrm{d}p_{\mathrm{T,ch\,jet}}\,\mathrm{d}\eta_{\mathrm{jet}}$ is the b-jet production cross
373 section in p–Pb, and $\mathrm{d}^2\sigma^{\mathrm{b\,jet}}_{\mathrm{pp}}/\mathrm{d}p_{\mathrm{T,ch\,jet}}\,\mathrm{d}\eta_{\mathrm{jet}}$ is b-jet production cross section in pp collisions.

4.5   Combining the results of the IP and SV methods

375 The p_{T}-differential b-jet production cross sections obtained from the IP and SV methods were combined
376 using the Best Linear Unbiased Estimator (BLUE) method [80, 81]. The BLUE method is used to
377 combine different measurements of the same physical quantity, where the uncertainties of the individual
378 measurements are correlated between the measurements to a given extent. Besides the b-jet cross section
379 in pp and p–Pb collisions, the BLUE method was also used to obtain the combined nuclear modification
380 factor $R^{\mathrm{b\text{-}jet}}_{\mathrm{pPb}}$ given that correlated systematic uncertainties cancel to a different degree in the individual
381 ratios for the IP and SV analyses.

382 The combined results were obtained under the following considerations. The systematic uncertainties
383 from tagging, background fluctuations, and the purity extraction were assumed to be uncorrelated be-
384 tween the two methods. The systematic contributions from the tracking efficiency and p_{T} resolution as
385 well as from the contamination by secondary tracks were treated as fully correlated. Since the same

dataset was used in the two methods, the statistical uncertainty is partially correlated. The correlation coefficient ρ_{stat} was estimated as

$$\rho_{\text{stat}} = \frac{\text{Cov(IP,SV)}}{\sigma_{\text{IP}}\sigma_{\text{SV}}} \quad \text{with} \quad \text{Cov(IP,SV)} = \frac{\sigma_{\text{IP}}^2\sigma_{\text{SV}}^2}{\sigma_{\text{IP}\cap\text{SV}}^2}, \tag{14}$$

where σ_{IP} (σ_{SV}) is the statistical uncertainty corresponding to the jet sample from the IP (SV) method, and $\sigma_{\text{IP}\cap\text{SV}}$ is the statistical uncertainty corresponding to the sample selected by both the IP and the SV methods. The correlation coefficients for statistical uncertainty are $\rho_{\text{stat}} = 0.35$ for pp collisions and $\rho_{\text{stat}} = 0.27$ for p–Pb collisions. For the unfolding uncertainties, which were partially correlated between both methods, an arbitrarily chosen correlation coefficient value of 0.5 was used, with values 0 and 1 as consistency checks. Correlation coefficients between other parameters were varied similarly and the resulting systematic uncertainty from these choices was found negligible.

5 Sources of systematic uncertainties

Systematic uncertainties of the p_{T}-differential b-jet cross-section and $R_{\text{pPb}}^{\text{b-jet}}$ were assessed by varying the selection and correction procedures. Table 1 lists the possible sources of systematic uncertainties, and the adopted variations, w.r.t. the standard selection procedures and methods used to obtain the central values of the results. These variations are discussed in more detail below. Table 2 then provides a summary of all uncertainties. The uncertainties are reported separately for the IP and SV analyses, as well as for the combined results obtained with the BLUE method. In the IP analysis, all uncertainties were considered as symmetrical, while in the SV analysis, most of the uncertainties were considered as asymmetrical. Systematic uncertainties due to the tracking efficiency and p_{T} resolution, tagging, contamination by secondary tracks, and background fluctuations were treated as fully correlated between the pp and p–Pb systems, hence these were partially propagated into $R_{\text{pPb}}^{\text{b-jet}}$, while the other uncertainties were considered uncorrelated and were fully propagated. The different types of correlated systematic uncertainties on the $R_{\text{pPb}}^{\text{b-jet}}$ were determined by the simultaneous variation of the pp and the p–Pb results to make sure that the correlations cancel out. Since the combination with the BLUE method requires symmetric uncertainties, two SV spectra were made, one with the lower and one with the upper uncertainties. These spectra were combined with the IP spectrum separately and a conservative choice was made by taking the maximum of the lower and upper boundaries point-by-point in the combined result. The individual uncertainty sources are discussed in detail in the following paragraphs.

5.1 Tracking efficiency

Systematic uncertainty on tracking efficiency is about 4% [82]. This uncertainty translates into an uncertainty on the energy scale of reconstructed jets. The resulting effect on the b-jet spectra was estimated by constructing an instrumental response matrix from which 4% of tracks were randomly dropped. This matrix represents the downward uncertainty on the reconstruction efficiency. It is assumed that a 4% variation towards higher tracking efficiency would affect the results symmetrically. The tracking efficiency uncertainty is one of the major sources of systematic uncertainties on the b-jet cross section. It tends to increase with increasing b-jet p_{T}.

5.2 p_{T} resolution of tracks

The p_{T} resolution of tracks was discussed briefly in Sec. 3 and more details can be found in Ref. [51]. The systematic uncertainty on track transverse momentum resolution was estimated from the azimuthal variation of $1/p_{\text{T}}$ spectrum shift of positively and negatively charged particles. The resulting effect of these variations on the b-jet cross section spectra was investigated by unfolding the spectra with an instrumental response matrix that reflected the observed local variations in p_{T} smearing.

Table 1: Summary of sources of systematic uncertainty and adopted variations to estimate their effects in case of the SV and the IP methods.

	Source		Standard analysis	Variations
Common	Tracking efficiency		default reconstruction	4% of tracks dropped
	Track p_T resolution		default reconstruction	p_T-smeared reconstruction
	Secondary track contamination		default MC correction	data-driven estimate
IP method	Underlying event fluctuations		RC tagged-jet events	RC inclusive-jet events
	Unfolding	Method	SVD	Bayesian–χ^2
		Regularization	8	7–9
		Matrix	full	truncated at 5 GeV/c
		Binning	default	limits shifted by 2 GeV/c
		Prior function	POWHEG b-jet spectrum	measured–unfolded χ^s spectra
	Tagging efficiency/purity	Sd_{xy}	2.5	1–4
		Fit distribution	$-\ln(JP)$	f_E
SV method	Underlying event fluctuations		embedding	random cone
	Tagging efficiency	SL_{xy}	7	6–8
		σ_{SV}	0.03 cm	0.02–0.05 cm
	Purity		POWHEG b and c spectra	"hybrid" scale variations
	Unfolding	Method	SVD	Bayesian
		Regularization	4	3–5
		Matrix	full	truncated at 5 GeV/c
		Binning	default	limits shifted with 1 GeV/c
		Prior function	POWHEG b-jet spectrum	all scale variations

Table 2: Statistical and systematic uncertainties, in per cent, corresponding to three representative $p_{\mathrm{T,chjet}}$ ranges for the pp and p–Pb cross sections as well as for the $R_{\mathrm{pPb}}^{\mathrm{b\text{-}jet}}$. Uncertainties of the IP and SV methods are quoted separately. Wherever applicable, the table also reports the resulting combined uncertainties. Both the upper and the lower values are listed for the asymmetric SV systematic uncertainties. An additional uncertainty from the normalization by the MB trigger cross sections [53, 54] is quoted in the last row.

$p_{\mathrm{T,chjet}}$ interval		10–20 GeV/c	40–50 GeV/c			80–100 GeV/c		
analysis		SV	IP	SV	comb.	IP	SV	comb.
Statistical uncertainty	pp	1.9	6.2	5.2	6.2	27.6	18.4	26.7
	p–Pb	1.9	6.4	3.6	6.7	14.5	12.9	15.0
	$R_{\mathrm{pPb}}^{\mathrm{b\text{-}jet}}$	2.6	8.9	6.4	5.8	31.2	22.5	20.5
Tracking efficiency	pp	7.9	11.1	8.4	11.1	15.6	9.5	15.3
	p–Pb	6.7	12.1	9.2	12.3	14.2	8.6	14.4
	$R_{\mathrm{pPb}}^{\mathrm{b\text{-}jet}}$	1.4	0.9	1.0	1.0	1.3	1.3	1.3
Tracking resolution	pp	$+1.2/-1.2$	1.2	$+3.9/-3.9$	1.2	2.9	$+6.0/-6.0$	3.1
	p–Pb	$+3.3/-3.3$	1.7	$+4.5/-4.5$	1.5	2.1	$+5.3/-5.3$	1.9
	$R_{\mathrm{pPb}}^{\mathrm{b\text{-}jet}}$	$+2.1/-2.2$	0.4	$+0.6/-0.6$	0.5	0.9	$+0.8/-0.7$	0.8
Secondary vertex contamination	pp	$+1.6/0$	2.2	$+2.4/0$	1.9	3.8	$+2.9/0$	8.2
	p–Pb	$+4.1/0$	6.2	$+5.4/0$	1.8	7.0	$+7.8/0$	3.0
	$R_{\mathrm{pPb}}^{\mathrm{b\text{-}jet}}$	$0/-2.5$	3.7	$0/-3.0$	3.2	3.0	$0/-5.1$	4.1
Background fluctuation	pp	$0/-5.4$	0.7	$0/-10.3$	0.8	0.4	$+3.2/0$	0.4
	p–Pb	$0/-3.1$	3.1	$0/-5.4$	3.3	2.0	$+3.1/0$	2.1
	$R_{\mathrm{pPb}}^{\mathrm{b\text{-}jet}}$	$+2.6/0$	2.5	$+6.7/0$	0.7	2.6	$+1.4/0$	1.3
b-jet tagging	pp	$+0.9/-2.8$	0.7	$+3.4/-6.5$	0.7	3.5	$+6.8/-13.4$	3.4
	p–Pb	$+3.4/-1.6$	1.1	$+4.6/-8.6$	1.2	0.5	$+6.0/-15.3$	0.6
	$R_{\mathrm{pPb}}^{\mathrm{b\text{-}jet}}$	$+2.5/-2.2$	1.3	$+5.0/-5.3$	3.9	3.5	$+10.7/-13.8$	7.3
Purity	pp	$+13.0/-21.8$	12.1	$+16.4/-16.8$	12.1	12.1	$+21.8/-17.3$	11.5
	p–Pb	$+13.1/-21.0$	9.0	$+11.9/-16.3$	9.4	9.0	$+21.1/-15.7$	9.4
	$R_{\mathrm{pPb}}^{\mathrm{b\text{-}jet}}$	$+5.2/-9.4$	14.8	$+5.2/-6.6$	6.3	14.8	$+8.2/-9.7$	8.8
Unfolding	pp	$+7.2/-0.9$	2.1	$+1.0/-1.9$	2.1	7.8	$+27.1/-6.1$	7.6
	p–Pb	$+9.5/-5.6$	0.9	$+0.5/-4.5$	0.8	1.6	$+11.4/-14.3$	1.5
	$R_{\mathrm{pPb}}^{\mathrm{b\text{-}jet}}$	$+2.5/-5.4$	2.3	$+3.1/-4.7$	3.8	7.9	$+4.4/-15.9$	10.6
Total systematic uncertainty	pp	$+17.0/-24.0$	16.7	$+19.3/-22.8$	16.7	22.0	$+37.4/-25.4$	22.6
	p–Pb	$+18.6/-23.2$	16.7	$+17.2/-22.2$	16.1	18.5	$+28.0/-28.1$	17.8
	$R_{\mathrm{pPb}}^{\mathrm{b\text{-}jet}}$	$+7.3/-11.6$	15.7	$+10.4/-10.2$	9.0	17.7	$+14.3/-23.8$	16.2
Normalization uncertainty	pp	2.3						
	p–Pb	3.5						
	$R_{\mathrm{pPb}}^{\mathrm{b\text{-}jet}}$	4.2						

5.3 Contamination from secondary tracks

Contamination of jets from secondary tracks due to weak decays was corrected for using the instrumental matrix. This correction is MC based and relies on the secondary track fractions from the simulations. As a systematic variation, these fractions were taken from a data driven approach where DCA distributions of tracks to the primary vertex were fitted with templates corresponding to primary tracks and

secondary tracks. This resulted in a systematic shift in jet energy scale. In the SV analysis this uncertainty was treated as one-sided since the true fraction of secondary tracks is expected to fall between the two calculations.

The production of long-lived strange particles are known not to be described accurately by the PYTHIA MC event generator [83–86]. Decays of K_S^0 and hyperons were however found to contribute by less than 1% to the constructed light-flavor SV invariant mass templates which are used for the data driven purity estimate. Possible variation of the strangeness in simulation would therefore have negligible impact on the shape of this template and therefore would have negligible impact on the extracted purity. A similar situation holds also for the IP templates where decays of long-lived strange particles contribute likewise on the percent level only. Omission of the long-lived strange particles from construction of the templates led to negligible changes of the fit results.

5.4 Underlying event fluctuations

In case of the SV method, this uncertainty was estimated by comparing the spectra unfolded using δp_T matrices constructed with the track embedding and the random cone method. This resulted in a one-sided uncertainty on the spectra. In the IP method, the RC method was used as the default estimator for the underlying event density fluctuation on events which have tagged jets, and the corresponding systematic uncertainty was obtained by considering δp_T matrices from inclusive events.

5.5 b-jet tagging efficiency and purity in the IP method

The uncertainty was estimated by varying the default impact parameter significance and template fit discriminator. The working point of the tagging selection criterion, set by default as $Sd_{xy}^{\min} = 2.5$, was varied in the range from 1 to 4. This resulted in variations in the data driven b-jet tagging efficiency and purity that were propagated to the b-jet cross sections.

Similarly, the default template fitting discriminator $-\ln(JP)$ was replaced with the energy fraction carried by the secondary vertex in the jet, f_E. Differences between these methods were added up in quadrature with the uncertainties from the fitting method to establish the overall uncertainty on the template fitting.

Purity of the selected b-jet candidates can be in principle affected also by the admixture of the long-lived strange V^0 particles (K_s^0 and $\Lambda/\bar{\Lambda}$), which result in decay-daughter tracks with large impact parameters. The possible effect of these daughter tracks on the purity and efficiency of the IP tagging was tested by ignoring those tracks that, when combined with other tracks of the same event, yield an invariant mass compatible with the K_s^0 or Λ hypothesis. The corresponding systematic effect on the resulting b-jet spectrum was found to be negligible.

5.6 b-jet tagging efficiency and purity in the SV method

The default tagging selection, $SL_{xy} > 7$ and $\sigma_{SV} < 0.03$ cm, was chosen to fall into a region where the simulation adequately describes data. The variations were done in a way that one of the parameters was kept at its default value while the other parameter was altered. In this study SL_{xy} was varied from 6 to 8 and σ_{SV} was varied from 0.02 to 0.05 cm. Since these two parameters are correlated, the envelope of the systematic variations is considered, constructed using the point-by-point maximal upper and lower variations.

In the SV method, the major source of systematic uncertainty on the b-jet cross sections stems from the purity assessment of the tagged b-jet candidate sample. The uncertainty was evaluated by repeating the analysis with each of the accepted POWHEG purity curves shown in Fig. 10. The uncertainty is defined by the envelope of the resulting spectrum variations.

The POWHEG configurations that provide a statistically acceptable description of the purity are determined based on template fits in the p–Pb system. Since the same configurations are used in the pp system, the assumptions on the CNM effects in POWHEG p–Pb simulations will, counter-intuitively, affect the purity estimation in the pp system. This effect was estimated based on the comparison of the POWHEG simulations to the existing heavy-flavor R_{pA} measurements [33, 47]. This additional, independent uncertainty on the SV-method purity in the pp system was found to be a couple of percents at low p_{T} and is vanishing towards higher p_{T}.

In the SV method, since a three-prong secondary vertex is required and the purity is determined based on template fitting of the invariant mass distribution, a possible incorrect modelling of V^0 particles is expected to pose negligible impact on the purity.

5.7   Unfolding

The IP and the SV method use SVD unfolding in the standard analysis. To establish the uncertainty stemming from the choice of the unfolding method, the spectra were also unfolded with the Bayesian method, and in the IP analysis, with the χ^2 method in addition. The sensitivity to the choice of regularization parameter was investigated by changing its value within ± 1. The unfolding was also repeated with a modified lower p_{T} limit of the input spectrum. The SV analysis considered also a different binning of the input p_{T} spectrum. Both methods used in their standard analysis the b-jet POWHEG spectrum as the default prior function. In the IP analysis, the unfolding was repeated using the measured, as well as the χ^2-unfolded spectra as priors. In the SV analysis, the unfolding was repeated by taking as priors the POWHEG b-jet spectra resulting from different scale and mass variations. Differences between these variations and the standard analysis spectra were added up in quadrature in the case of the IP analysis. In the SV analysis, the statistical and systematic parts were separated using pseudo-experiments with randomized input spectra. The pseudo-experiments were carried out for the standard analysis configuration as well as for each systematic variation. The maximum deviations at each $p_{\mathrm{T,chjet}}$ value were taken as asymmetric uncertainties.

An additional systematic uncertainty stems from the limited knowledge of very low momentum jet-production, determined from PYTHIA simulations when constructing the response matrix. This was estimated by using a matrix that was truncated below $p_{\mathrm{T,chjet}} = 5\,\mathrm{GeV}/c$, and the resulting deviation w.r.t. the standard analysis spectrum was added up in quadrature to the total uncertainty.

6   Results and discussion

6.1   b-jet production cross section in pp and p–Pb collisions

Figure 11 presents the p_{T}-differential production cross section of b jets obtained from the IP and SV analyses in pp and p–Pb collisions at $\sqrt{s_{\mathrm{NN}}} = 5.02\,\mathrm{TeV}$. For easier comparison across the two systems, the p–Pb cross section is normalized by the number of Pb nucleons $A = 208$. The results obtained with the two methods are consistent within the uncertainties.

The combined b-jet cross sections are compared with NLO pQCD calculations by the POWHEG dijet tune with PYTHIA 8 fragmentation [87, 88], see Fig. 12. The measured b-jet cross section is in agreement with the calculations within the experimental and theoretical uncertainties. The quoted theoretical uncertainties on the POWHEG data contain uncertainties obtained by changing the renormalization and factorization scales by a factor 0.5–2, variation of α_s, and variation of the PDFs of the CT14NLO parton distribution function [89] and the EPPS16 nPDF [90] in the POWHEG calculations. The CT14NLO and EPPS16 uncertainties were propagated according to the Hessian prescription of the authors of these parameterizations (Eq. 53 of Ref. [90]). The uncertainty on α_s was estimated by varying the strong coupling from 0.111 to 0.123.
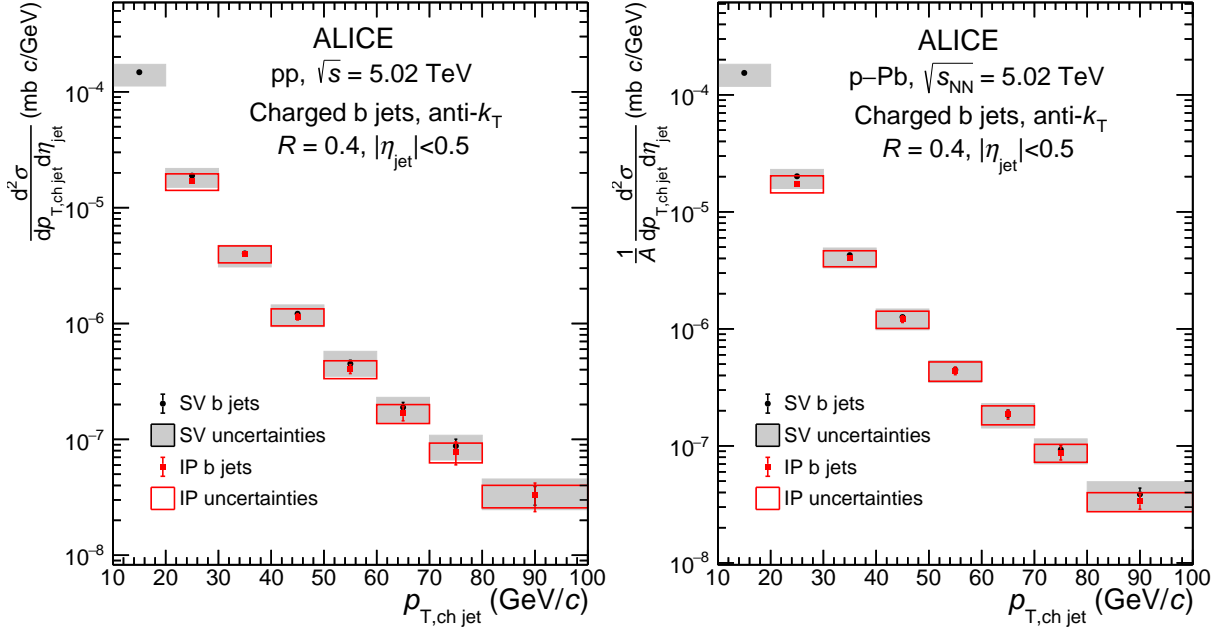
Figure 11: Comparison of the p_T differential production cross section of charged-particle anti-k_T $R = 0.4$ b jets measured in pp and p–Pb collisions at $\sqrt{s_{NN}} = 5.02$ TeV using the IP and SV methods. Systematic and statistical uncertainties are shown as boxes and error bars, respectively.
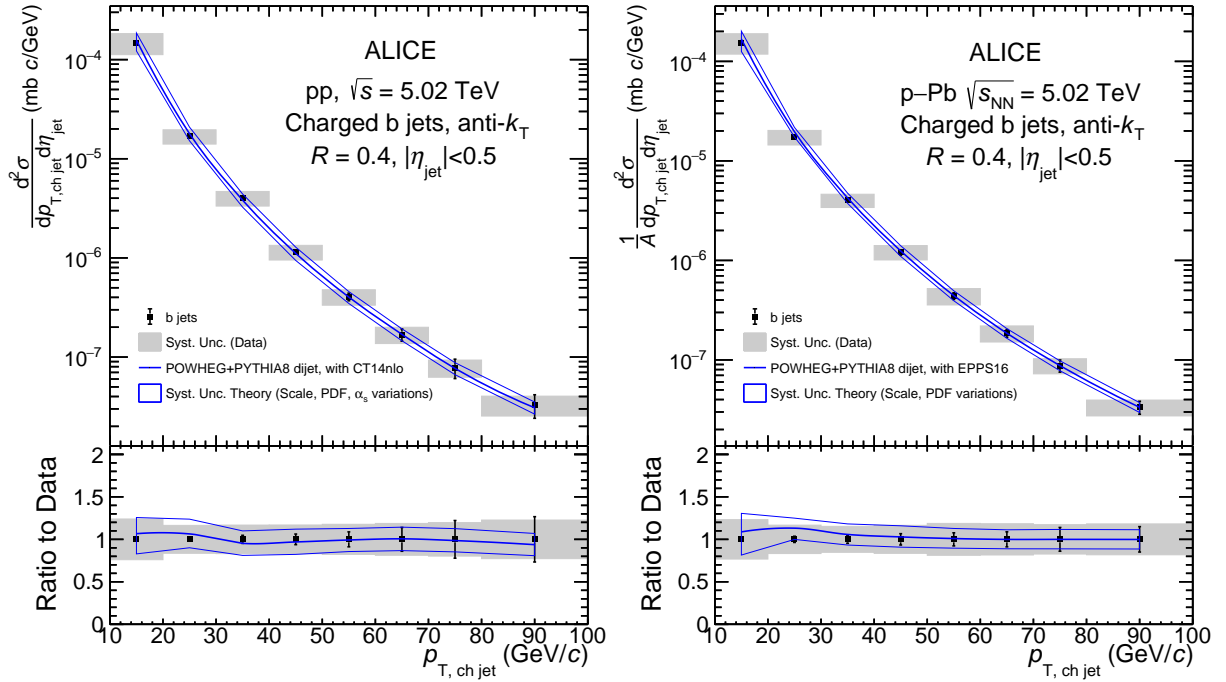

Figure 12: Top panels: The combined differential production cross section of charged-particle anti-k_T $R = 0.4$ b jets measured in pp (left) and p–Pb (right) collisions at $\sqrt{s_{NN}} = 5.02$ TeV. The data are compared to NLO pQCD prediction by the POWHEG dijet tune with PYTHIA 8 fragmentation [87, 88]. Systematic and statistical uncertainties are shown as boxes and error bars, respectively. Bottom panels: ratio of theory calculations to the data. There is an additional normalization uncertainty of 3.5% on the p–Pb spectra, and 2.3% on the pp spectra.

6.2   b-jet fraction

Figure 13 shows the fraction of charged-particle b-jets among inclusive charged-particle jets in the pp and p–Pb systems. The reference p_T differential production cross sections of the inclusive charged-particle jets in pp and p–Pb were taken from Refs. [91] and [92], respectively. The inclusive-jet and the b-jet measurements were obtained from different data samples, collected in different periods. Although a part of the uncertainties corresponding to track reconstruction may be correlated, as a conservative approach both the statistical and systematic uncertainties of the inclusive and b-jet cross sections were considered as uncorrelated. The measured b-jet fractions are compared with calculations of the POWHEG dijet tune with PYTHIA 8 fragmentation [87, 88]. The measured b-jet fraction is consistent with these predictions within the uncertainties.
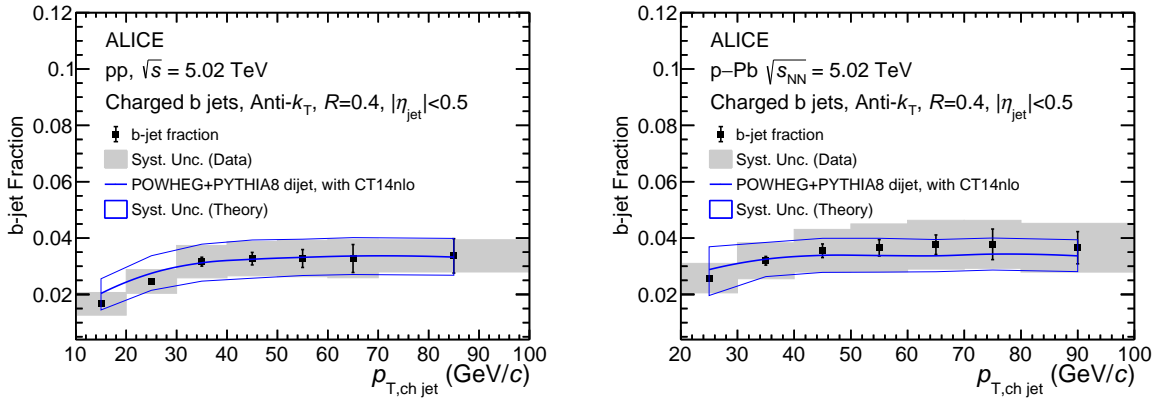

Figure 13: The b-jet fraction in pp collisions at $\sqrt{s}$ = 5.02 TeV (left) and p–Pb collisions at $\sqrt{s_{NN}}$ = 5.02 TeV (right), compared to POWHEG NLO pQCD calculations with PYTHIA 8 fragmentation.

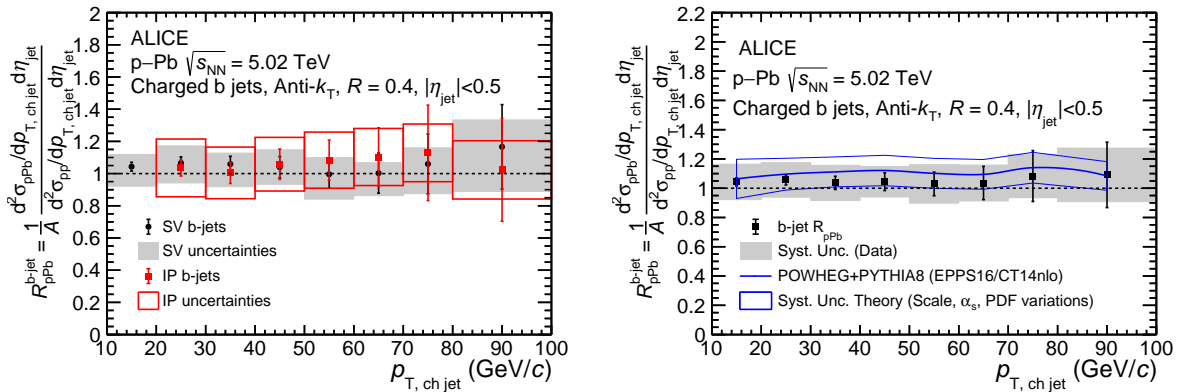## 6.3   The b-jet nuclear modification factor $R_{pPb}^{b\text{-}jet}$

Figure 14: Left: The nuclear modification factor $R_{pPb}^{b\text{-}jet}$ of the inclusive charged-particle anti-k_T $R = 0.4$ b jets as a function of p_T from the IP and SV method. Right: The nuclear modification factor $R_{pPb}^{b\text{-}jet}$ obtained from combining the IP and SV method results as a function of $p_{T,ch\,jet}$ compared to the calculation by the POWHEG dijet tune with the PYTHIA 8 fragmentation [87, 88]. Systematic and statistical uncertainties are shown as boxes and error bars, respectively. There is an additional normalization uncertainty of 4.2%.

Figure 14 (left) shows the nuclear modification factor of charged-particle b jets obtained from the IP and SV methods. The $R_{pPb}^{b\text{-}jet}$ of the two methods are consistent within uncertainties. Figure 14 (right) displays

the combined b-jet nuclear modification factor $R_{\mathrm{pPb}}^{\mathrm{b\text{-}jet}}$ as a function of $p_{\mathrm{T,chjet}}$, compared to the NLO
pQCD, POWHEG dijet tune with PYTHIA 8 fragmentation calculations [87, 88]. The $R_{\mathrm{pPb}}^{\mathrm{b\text{-}jet}}$ is consistent
with unity within the uncertainties in the full $10 < p_{\mathrm{T,chjet}} < 100\,\mathrm{GeV}/c$ range of the measurement. The
pQCD calculations describe the data within uncertainties. These results indicate that there is no strong
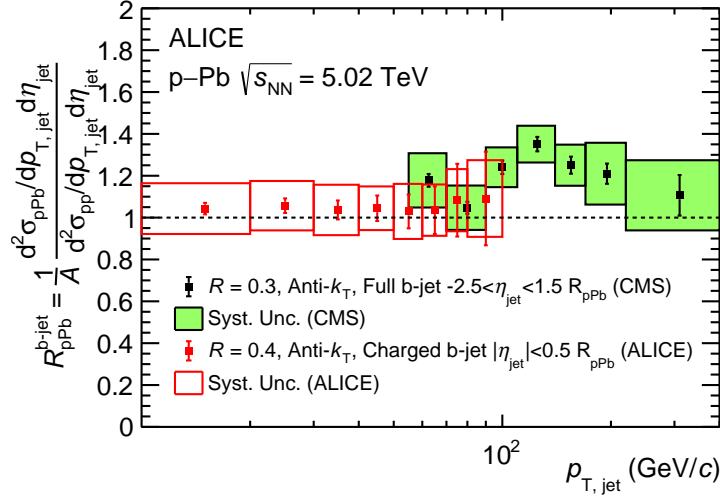nuclear matter effect present in b-jet production in p–Pb collisions at $\sqrt{s_{\mathrm{NN}}} = 5.02$ TeV.

Figure 15: The nuclear modification factor $R_{\mathrm{pPb}}^{\mathrm{b\text{-}jet}}$ for charged-particle b jets measured by the ALICE ex-
periment, compared with the b-jet measurement from the CMS experiment [67]. The CMS measurement
represents $R = 0.3$ fully reconstructed b jets within $-2.5 < \eta_{\mathrm{jet}} < 1.5$. There is an additional $\approx 22\%$
scaling uncertainty from the PYTHIA pp reference on the CMS data that is not shown in the figure.

Figure 15 shows the $R_{\mathrm{pPb}}^{\mathrm{b\text{-}jet}}$ for charged-particle b-jets measured by ALICE as a function of p_{T}, compared
with the measurement of the CMS collaboration for full-jet b jets [67]. Since the jets from CMS also
include the neutral particles, the p_{T} scales do not compare directly. Note that there is an additional
$\approx 22\%$ scaling uncertainty on the CMS data from the pp reference that was computed using PYTHIA
simulations. Despite the different jet definitions and rapidity ranges used in the two measurements, the
ALICE and CMS data are fully compatible in the overlap region. A substantial nuclear modification of
b-jet production by the cold nuclear matter can be excluded in the whole range from $p_{\mathrm{T,chjet}} > 10\,\mathrm{GeV}/c$
(approximately corresponding to $p_{\mathrm{T,fulljet}} \gtrsim 15\,\mathrm{GeV}/c$) up to $p_{\mathrm{T,fulljet}} < 400\,\mathrm{GeV}/c$.

7 Summary

In this paper, we presented the measurement of the p_{T}-differential b-jet production cross sections in pp
collisions and p–Pb collisions at $\sqrt{s_{\mathrm{NN}}} = 5.02$ TeV in the transverse momentum range $10 \leq p_{\mathrm{T,chjet}} \leq$
$100\,\mathrm{GeV}/c$. The measured cross sections were used to determine the b-jet fractions in pp and p–Pb and
to evaluate the b-jet nuclear modification factor $R_{\mathrm{pPb}}^{\mathrm{b\text{-}jet}}$ in p–Pb collisions down to a $p_{\mathrm{T,chjet}}$ of $10\,\mathrm{GeV}/c$.
Within the current precision, the $R_{\mathrm{pPb}}^{\mathrm{b\text{-}jet}}$ is found to be consistent with unity, implying no strong cold
nuclear effects on the b-jet production in p–Pb collisions at $\sqrt{s_{\mathrm{NN}}} = 5.02$ TeV. The b-jet measurements
are found to be in agreement with the NLO pQCD POWHEG calculations with PYTHIA 8 fragmentation
within the uncertainties.

In the low jet transverse momentum range, jet energy loss by radiative and collisional mechanisms in a
hot and dense medium is expected to be strongly mass dependent. The current results that exploit the
excellent tracking capabilities of ALICE and reach down to $p_{\mathrm{T,chjet}} = 10\,\mathrm{GeV}/c$, provide a baseline for
future measurements of nuclear modification in heavy-ion collisions.

Acknowledgements

References

[1] N. Cabibbo and G. Parisi, "Exponential hadronic spectrum and quark liberation", *Phys. Lett. B* **59** (1975) .

[2] G. Chapline and M. Nauenberg, "Asymptotic Freedom and the Baryon-Quark Phase Transition", *Phys. Rev. D* **16** (1977) .

[3] E. V. Shuryak, "Quark-Gluon Plasma and Hadronic Production of Leptons, Photons and Psions", *Sov. J. Nucl. Phys.* **28** (1978) .

[4] **STAR** Collaboration, J. Adams *et al.*, "Experimental and theoretical challenges in the search for the quark gluon plasma: The STAR Collaboration's critical assessment of the evidence from RHIC collisions", *Nucl. Phys. A* **757** (2005) , `arXiv:nucl-ex/0501009`.

[5] **PHENIX** Collaboration, K. Adcox *et al.*, "Formation of dense partonic matter in relativistic nucleus-nucleus collisions at RHIC: Experimental evaluation by the PHENIX collaboration", *Nucl. Phys. A* **757** (2005) , `arXiv:nucl-ex/0410003`.

[6] **BRAHMS** Collaboration, I. Arsene *et al.*, "Quark gluon plasma and color glass condensate at RHIC? The Perspective from the BRAHMS experiment", *Nucl. Phys. A* **757** (2005) , `arXiv:nucl-ex/0410020`.

[7] **PHOBOS** Collaboration, B. B. Back *et al.*, "The PHOBOS perspective on discoveries at RHIC", *Nucl. Phys. A* **757** (2005) , `arXiv:nucl-ex/0410022`.

[8] A. Ali and G. Kramer, "Jets and QCD: A Historical Review of the Discovery of the Quark and Gluon Jets and its Impact on QCD", *Eur. Phys. J. H* **36** (2011) , `arXiv:1012.2288 [hep-ph]`.

[9] A. Majumder and M. Van Leeuwen, "The Theory and Phenomenology of Perturbative QCD Based Jet Quenching", *Prog. Part. Nucl. Phys.* **66** (2011) , `arXiv:1002.2206 [hep-ph]`.

[10] M. Gyulassy, P. Levai, and I. Vitev, "Jet quenching in thin quark gluon plasmas. 1. Formalism", *Nucl. Phys. B* **571** (2000) , `arXiv:hep-ph/9907461`.

[11] E. Wang and X.-N. Wang, "Jet tomography of dense and nuclear matter", *Phys. Rev. Lett.* **89** (2002) , `arXiv:hep-ph/0202105`.

[12] **PHENIX** Collaboration, K. Adcox *et al.*, "Suppression of hadrons with large transverse momentum in central Au+Au collisions at $\sqrt{s_{NN}} = 130\,\mathrm{GeV}$", *Phys. Rev. Lett.* **88** (2002) , `arXiv:nucl-ex/0109003`.

[13] **ALICE** Collaboration, K. Aamodt *et al.*, "Suppression of Charged Particle Production at Large Transverse Momentum in Central Pb–Pb Collisions at $\sqrt{s_{NN}} = 2.76\,\mathrm{TeV}$", *Phys. Lett. B* **696** (2011) , `arXiv:1012.1004 [nucl-ex]`.

[14] **CMS** Collaboration, S. Chatrchyan *et al.*, "Study of high-pT charged particle suppression in PbPb compared to *pp* collisions at $\sqrt{s_{NN}} = 2.76\,\mathrm{TeV}$", *Eur. Phys. J. C* **72** (2012) , `arXiv:1202.2554 [nucl-ex]`.

[15] **CMS** Collaboration, A. M. Sirunyan *et al.*, "Measurement of the Splitting Function in *pp* and Pb–Pb Collisions at $\sqrt{s_{NN}} = 5.02\,\mathrm{TeV}$", *Phys. Rev. Lett.* **120** no. 14, (2018) , `arXiv:1708.09429 [nucl-ex]`.

[16] **ALICE** Collaboration, S. Acharya *et al.*, "Exploration of jet substructure using iterative declustering in pp and Pb–Pb collisions at LHC energies", *Phys. Lett. B* **802** (2020) , arXiv:1905.02512 [nucl-ex].

[17] G. Milhano, U. A. Wiedemann, and K. C. Zapp, "Sensitivity of jet substructure to jet-induced medium response", *Phys. Lett. B* **779** (2018) , arXiv:1707.04142 [hep-ph].

[18] Y. Mehtar-Tani and K. Tywoniuk, "Groomed jets in heavy-ion collisions: sensitivity to medium-induced bremsstrahlung", *JHEP* **04** (2017) , arXiv:1610.08930 [hep-ph].

[19] H. Fujii and K. Watanabe, "Heavy quark pair production in high energy pA collisions: Open heavy flavors", *Nucl. Phys. A* **920** (2013) , arXiv:1308.1258 [hep-ph].

[20] M. L. Mangano, P. Nason, and G. Ridolfi, "Heavy quark correlations in hadron collisions at next-to-leading order", *Nucl. Phys. B* **373** (1992) .

[21] R. Sharma, I. Vitev, and B.-W. Zhang, "Light-cone wave function approach to open heavy flavor dynamics in QCD matter", *Phys. Rev. C* **80** (2009) , arXiv:0904.0032 [hep-ph].

[22] Z.-B. Kang, I. Vitev, E. Wang, H. Xing, and C. Zhang, "Multiple scattering effects on heavy meson production in p+*A* collisions at backward rapidity", *Phys. Lett. B* **740** (2015) , arXiv:1409.2494 [hep-ph].

[23] **CMS** Collaboration, V. Khachatryan *et al.*, "Observation of Long-Range Near-Side Angular Correlations in Proton-Proton Collisions at the LHC", *JHEP* **09** (2010) , arXiv:1009.4122 [hep-ex].

[24] **ALICE** Collaboration, B. Abelev *et al.*, "Long-range angular correlations on the near and away side in *p*–Pb collisions at $\sqrt{s_{NN}} = 5.02$ TeV", *Phys. Lett. B* **719** (2013) , arXiv:1212.2001 [nucl-ex].

[25] **PHENIX** Collaboration, C. Aidala *et al.*, "Creation of quark–gluon plasma droplets with three distinct geometries", *Nature Phys.* **15** no. 3, (2019) , arXiv:1805.02973 [nucl-ex].

[26] L. Yan and J.-Y. Ollitrault, "Universal fluctuation-driven eccentricities in proton-proton, proton-nucleus and nucleus-nucleus collisions", *Phys. Rev. Lett.* **112** (2014) , arXiv:1312.6555 [nucl-th].

[27] C. Bierlich, G. Gustafson, and L. Lönnblad, "Collectivity without plasma in hadronic collisions", *Phys. Lett. B* **779** (2018) , arXiv:1710.09725 [hep-ph].

[28] B. Blok, C. D. Jäkel, M. Strikman, and U. A. Wiedemann, "Collectivity from interference", *JHEP* **12** (2017) , arXiv:1708.08241 [hep-ph].

[29] T. A. Trainor, "Questioning quark-gluon plasma formation in small collision systems", arXiv:1905.11585 [hep-ph].

[30] **ALICE** Collaboration, S. Acharya *et al.*, "Constraints on jet quenching in p–Pb collisions at $\sqrt{s_{NN}} = 5.02$ TeV measured by the event-activity dependence of semi-inclusive hadron-jet distributions", *Phys. Lett. B* **783** (2018) , arXiv:1712.05603 [nucl-ex].

[31] **ALICE** Collaboration, S. Acharya *et al.*, "Transverse momentum spectra and nuclear modification factors of charged particles in pp, p–Pb and Pb–Pb collisions at the LHC", *JHEP* **11** (2018) , arXiv:1802.09145 [nucl-ex].

[32] **ALICE** Collaboration, J. Adam *et al.*, "Centrality dependence of particle production in p–Pb collisions at $\sqrt{s_{NN}} = 5.02$ TeV", *Phys. Rev. C* **91** (2015) , `arXiv:1412.6828 [nucl-ex]`.

[33] **ALICE** Collaboration, S. Acharya *et al.*, "Measurement of prompt D^0, D^+, D^{*+}, and D_s^+ production in p–Pb collisions at $\sqrt{s_{NN}} = 5.02$ TeV", *JHEP* **12** (2019) , `arXiv:1906.03425 [nucl-ex]`.

[34] A. Buzzatti and M. Gyulassy, "Jet Flavor Tomography of Quark Gluon Plasmas at RHIC and LHC", *Phys. Rev. Lett.* **108** (2012) , `arXiv:1106.3061 [hep-ph]`.

[35] M. Djordjevic and M. Djordjevic, "LHC jet suppression of light and heavy flavor observables", *Phys. Lett. B* **734** (2014) , `arXiv:1307.4098 [hep-ph]`.

[36] X. Dong, Y.-J. Lee, and R. Rapp, "Open Heavy-Flavor Production in Heavy-Ion Collisions", *Ann. Rev. Nucl. Part. Sci.* **69** (2019) , `arXiv:1903.07709 [nucl-ex]`.

[37] W.-J. Xing, S. Cao, G.-Y. Qin, and H. Xing, "Flavor hierarchy of jet quenching in relativistic heavy-ion collisions", *Phys. Lett. B* **805** (2020) , `arXiv:1906.00413 [hep-ph]`.

[38] **ALICE** Collaboration, S. Acharya *et al.*, "Azimuthal Anisotropy of Heavy-Flavor Decay Electrons in p–Pb collisions at $\sqrt{s} = 5.02$ TeV", *Phys. Rev. Lett.* **122** (2019) , `arXiv:1805.04367 [nucl-ex]`.

[39] **CMS** Collaboration, A. Sirunyan *et al.*, "Measurement of Prompt D^0 Meson Azimuthal Anisotropy in Pb–Pb Collisions at $\sqrt{s} = 5.02$ TeV", *Phys. Rev. Lett.* **120** (2018) , `arXiv:1708.03497 [nucl-ex]`.

[40] Y. L. Dokshitzer, V. A. Khoze, and S. I. Troian, "On specific QCD properties of heavy quark fragmentation ('dead cone')", *J. Phys. G* **17** (1991) .

[41] A. Andronic *et al.*, "Heavy-flavour and quarkonium production in the LHC era: from proton–proton to heavy-ion collisions", *Eur. Phys. J. C* **76** no. 3, (2016) , `arXiv:1506.03981 [nucl-ex]`.

[42] N. Armesto, C. A. Salgado, and U. A. Wiedemann, "Medium induced gluon radiation off massive quarks fills the dead cone", *Phys. Rev. D* **69** (2004) , `arXiv:hep-ph/0312106`.

[43] **ALICE** Collaboration, B. Abelev *et al.*, "Suppression of high transverse momentum D mesons in central Pb–Pb collisions at $\sqrt{s_{NN}} = 2.76$ TeV", *JHEP* **09** (2012) , `arXiv:1203.2160 [nucl-ex]`.

[44] **CMS** Collaboration, S. Chatrchyan *et al.*, "Suppression of non-prompt J/ψ, prompt J/ψ, and Y(1S) in PbPb collisions at $\sqrt{s_{NN}} = 2.76$ TeV", *JHEP* **05** (2012) , `arXiv:1201.5069 [nucl-ex]`.

[45] **ALICE** Collaboration, S. Acharya *et al.*, "Measurements of low-p_T electrons from semileptonic heavy-flavour hadron decays at mid-rapidity in pp and Pb–Pb collisions at $\sqrt{s_{NN}} = 2.76$ TeV", *JHEP* **10** (2018) , `arXiv:1805.04379 [nucl-ex]`.

[46] **CMS** Collaboration, A. M. Sirunyan *et al.*, "Measurements of the charm jet cross section and nuclear modification factor in pPb collisions at $\sqrt{s_{NN}} = 5.02$ TeV", *Phys. Lett.* **B772** (2017) , `arXiv:1612.08972 [nucl-ex]`.

[47] **ALICE** Collaboration, S. Acharya *et al.*, "Measurement of electrons from heavy-flavour hadron decays as a function of multiplicity in p–Pb collisions at $\sqrt{s_{NN}} = 5.02$ TeV", *JHEP* **02** (2020) , `arXiv:1910.14399 [nucl-ex]`.

[48] **ALICE** Collaboration, S. Acharya *et al.*, "Measurement of the production of charm jets tagged with D^0 mesons in pp collisions at $\sqrt{s} = 7$ TeV", *JHEP* **08** (2019) , `arXiv:1905.02510` `[nucl-ex]`.

[49] **CMS** Collaboration, S. Chatrchyan *et al.*, "Evidence of b-Jet Quenching in PbPb Collisions at $\sqrt{s_{NN}} = 2.76$ TeV", *Phys. Rev. Lett.* **113** no. 13, (2014) , `arXiv:1312.4198` `[nucl-ex]`. [Erratum: Phys.Rev.Lett. 115, 029903 (2015)].

[50] **ALICE** Collaboration, K. Aamodt *et al.*, "The ALICE experiment at the CERN LHC", *JINST* **3** (2008) .

[51] **ALICE** Collaboration, B. Abelev *et al.*, "Performance of the ALICE Experiment at the CERN LHC", *Int. J. Mod. Phys. A* **A29** (2014) .

[52] **ALICE** Collaboration, E. Abbas *et al.*, "Performance of the ALICE VZERO system", *JINST* **8** (2013) , `arXiv:1306.3130` `[nucl-ex]`.

[53] **ALICE** Collaboration, B. B. Abelev *et al.*, "Measurement of visible cross sections in proton-lead collisions at $\sqrt{s_{NN}} = 5.02$ TeV in van der Meer scans with the ALICE detector", *JINST* **9** no. 11, (2014) , `arXiv:1405.1849` `[nucl-ex]`.

[54] **ALICE** Collaboration, "ALICE luminosity determination for pp collisions at $\sqrt{s} = 5$ TeV",. `https://cds.cern.ch/record/2202638`.

[55] M. Cacciari, G. P. Salam, and G. Soyez, "The Anti-k(t) jet clustering algorithm", *JHEP* **04** (2008) , `arXiv:0802.1189` `[hep-ph]`.

[56] M. Cacciari, G. P. Salam, and G. Soyez, "FastJet User Manual", *Eur. Phys. J. C* **72** (2012) , `arXiv:1111.6097` `[hep-ph]`.

[57] **CMS** Collaboration, S. Chatrchyan *et al.*, "Shape, Transverse Size, and Charged Hadron Multiplicity of Jets in pp Collisions at 7 TeV", *JHEP* **06** (2012) , `arXiv:1204.3170` `[hep-ex]`.

[58] M. Cacciari and G. P. Salam, "Pileup subtraction using jet areas", *Phys.Lett.B* **659** (2008) , `arXiv:0707.1378` `[hep-ph]`.

[59] **CMS** Collaboration, S. Chatrchyan *et al.*, "Measurement of the underlying event activity in pp collisions at $\sqrt{s} = 0.9$ and 7 TeV with the novel jet-area/median approach", *JHEP* **08** (2012) , `arXiv:1207.2392` `[hep-ex]`.

[60] G. P. Salam, "Towards Jetography", *Eur. Phys. J.* **C67** (2010) , `arXiv:0906.1833` `[hep-ph]`.

[61] **CMS** Collaboration, S. Chatrchyan *et al.*, "Identification of b-quark jets with the CMS experiment", *JINST* **8** (2013) , `arXiv:1211.4462` `[hep-ex]`.

[62] J. Montejo Berlingen, *Reconstruction of Physics Objects*, pp. 61–85. Springer International Publishing, Cham, 2016. `https://doi.org/10.1007/978-3-319-41051-7_4`.

[63] **D0** Collaboration, V. M. Abazov *et al.*, "*b*-Jet Identification in the D0 Experiment", *Nucl. Instrum. Meth.* **A620** (2010) , `arXiv:1002.4224` `[hep-ex]`.

[64] P. Skands, S. Carrazza, and J. Rojo, "Tuning PYTHIA 8.1: the Monash 2013 Tune", *Eur. Phys. J. C* **74** no. 8, (2014) , `arXiv:1404.5630` `[hep-ph]`.

[65] R. Brun, F. Bruyant, F. Carminati, S. Giani, M. Maire, A. McPherson, G. Patrick, and L. Urban, "GEANT Detector Description and Simulation Tool", *CERN-W5013* (10, 1994) .

[66] **DELPHI** Collaboration, J. Abdallah *et al.*, "b tagging in DELPHI at LEP", *Eur. Phys. J. C* **32** (2004) , `arXiv:hep-ex/0311003`.

[67] **CMS** Collaboration, V. Khachatryan *et al.*, "Transverse momentum spectra of inclusive b jets in pPb collisions at $\sqrt{s_{NN}} = 5.02\,\text{TeV}$", *Phys. Lett.* **B754** (2016) , `arXiv:1510.03373 [nucl-ex]`.

[68] T. Pierog, I. Karpenko, J. M. Katzy, E. Yatsenko, and K. Werner, "EPOS LHC: Test of collective hadronization with data measured at the CERN Large Hadron Collider", *Phys. Rev.* **C92** no. 3, (2015) , `arXiv:1306.0121 [hep-ph]`.

[69] **ALICE** Collaboration, S. Acharya *et al.*, "First measurement of jet mass in Pb–Pb and p–Pb collisions at the LHC", *Phys. Lett. B* **776** (2018) , `arXiv:1702.00804 [nucl-ex]`.

[70] S. Frixione, P. Nason, , and G. Ridolf, "A Positive-weight next-to-leading-order Monte Carlo for heavy flavour hadroproduction", *JHEP* **0709** (2007) , `arXiv:0707.3088 [hep-ph]`.

[71] J. Pumplin, D. R. Stump, J. Huston, H. L. Lai, P. M. Nadolsky, and W. K. Tung, "New generation of parton distributions with uncertainties from global QCD analysis", *JHEP* **07** (2002) , `arXiv:hep-ph/0201195`.

[72] K. J. Eskola, H. Paukkunen, and C. A. Salgado, "EPS09: A New Generation of NLO and LO Nuclear Parton Distribution Functions", *JHEP* **04** (2009) , `arXiv:0902.4154 [hep-ph]`.

[73] **ALICE** Collaboration, J. Adam *et al.*, "Measurement of jet suppression in central Pb–Pb collisions at $\sqrt{s_{NN}} = 2.76\,\text{TeV}$", *Phys. Lett. B* **746** (2015) , `arXiv:1502.01689 [nucl-ex]`.

[74] T. Sjostrand, S. Mrenna, and P. Z. Skands, "PYTHIA 6.4 Physics and Manual", *JHEP* **05** (2006) , `arXiv:hep-ph/0603175`.

[75] **ALICE** Collaboration, B. Abelev *et al.*, "Measurement of charged jet suppression in Pb-Pb collisions at $\sqrt{s_{NN}} = 2.76\,\text{TeV}$", *JHEP* **03** (2014) , `arXiv:1311.0633 [nucl-ex]`.

[76] **ALICE** Collaboration, B. Abelev *et al.*, "Measurement of Event Background Fluctuations for Charged Particle Jet Reconstruction in Pb–Pb collisions at $\sqrt{s_{NN}} = 2.76\,\text{TeV}$", *JHEP* **03** (2012) , `arXiv:1201.2423 [hep-ex]`.

[77] A. Hocker and V. Kartvelishvili, "SVD approach to data unfolding", *Nucl. Instrum. Meth.* **A372** (1996) , `arXiv:hep-ph/9509307 [hep-ph]`.

[78] T. Adye, "Unfolding algorithms and tests using RooUnfold", in *PHYSTAT 2011*, pp. 313–318. CERN, Geneva, 2011. `arXiv:1105.1160 [physics.data-an]`.

[79] G. D'Agostini, "Bayesian inference in processing experimental data: principles and basic applications", *Reports on Progress in Physics* **66** (Sept., 2003) , `physics/0304102`.

[80] L. Lyons, D. Gibaut, and P. Clifford, "How to Combine Correlated Estimates of a Single Physical Quantity", *Nucl. Instrum. Meth. A* **270** (1988) .

[81] A. Valassi, "Combining correlated measurements of several different physical quantities", *Nucl. Instrum. Meth. A* **500** (2003) .

[82] **ALICE** Collaboration, S. Acharya *et al.*, "Measurements of inclusive jet spectra in pp and central Pb–Pb collisions at $\sqrt{s_{NN}} = 5.02\,\text{TeV}$", *Phys. Rev. C* **101** no. 3, (2020) , `arXiv:1909.09718 [nucl-ex]`.

[83] **ALICE** Collaboration, S. Acharya *et al.*, "Production of light-flavor hadrons in pp collisions at $\sqrt{s} = 7\,\text{TeV}$ and $\sqrt{s} = 13\,\text{TeV}$", *Eur. Phys. J. C* **81** (2021) , `arXiv:2005.11120 [nucl-ex]`.

[84] **ALICE** Collaboration, K. Aamodt *et al.*, "Production of pions, kaons and protons in pp collisions at $\sqrt{s} = 900$ GeV with ALICE at the LHC", *Eur. Phys. J. C* **71** (2011) , arXiv:1101.4110 [nucl-ex].

[85] **CMS** Collaboration, S. Chatrchyan *et al.*, "Study of the inclusive production of charged pions, kaons, and protons in pp collisions at $\sqrt{s} = 0.9, 2.76$, and 7 TeV", *Eur. Phys. J. C* **72** (2012) , arXiv:1207.4724 [nucl-ex].

[86] **ALICE** Collaboration, B. Abelev *et al.*, "Multi-strange baryon production in pp collisions at $\sqrt{s} = 7$ TeV with ALICE", *Phys. Lett. B* **712** (2012) , arXiv:1204.0282 [nucl-ex].

[87] S. Alioli, K. Hamilton, P. Nason, C. Oleari, and E. Re, "Jet pair production in POWHEG", *JHEP* **04** (2011) , arXiv:1012.3380 [hep-ph].

[88] S. Frixione, P. Nason, and C. Oleari, "Matching NLO QCD computations with Parton Shower simulations: the POWHEG method", *JHEP* **11** (2007) , arXiv:0709.2092 [hep-ph].

[89] S. Dulat, T.-J. Hou, J. Gao, M. Guzzi, J. Huston, P. Nadolsky, J. Pumplin, C. Schmidt, D. Stump, and C. P. Yuan, "New parton distribution functions from a global analysis of quantum chromodynamics", *Phys. Rev.* **D93** no. 3, (2016) , arXiv:1506.07443 [hep-ph].

[90] K. J. Eskola, P. Paakkinen, H. Paukkunen, and C. A. Salgado, "EPPS16: Nuclear parton distributions with LHC data", *Eur. Phys. J.* **C77** no. 3, (2017) , arXiv:1612.05741 [hep-ph].

[91] **ALICE** Collaboration, S. Acharya *et al.*, "Measurement of charged jet cross section in pp collisions at $\sqrt{s} = 5.02$ TeV", *Phys. Rev.* **D100** no. 9, (2019) , arXiv:1905.02536 [nucl-ex].

[92] **ALICE** Collaboration, J. Adam *et al.*, "Measurement of charged jet production cross sections and nuclear modification in p–Pb collisions at $\sqrt{s_{NN}} = 5.02$ TeV", *Phys. Lett.* **B749** (2015) , arXiv:1503.00681 [nucl-ex].

777 **A   The ALICE Collaboration**